Journal of Sound and Vibration 531 (2022) 116714

Contents lists available at ScienceDirect

Journal of Sound and Vibration

journal homepage: www.elsevier.com/locate/jsvi

Experiments on aerothermoelastic fluid–structure interaction in hypersonic flow

Dennis Daub *, Sebastian Willems, Ali Gülhan

Deutsches Zentrum für Luft- und Raumfahrt e.V. (DLR), Institute of Aerodynamics and Flow Technology, Supersonic and Hypersonic Technology Department, Linder Höhe, 51147 Köln, Germany

ARTICLE INFO

Keywords:
Fluid–structure interaction
Flutter
Aerothermodynamics
Thermal buckling
Shock-wave/boundary-layer interaction
Hypersonic flow
Structural failure

ABSTRACT

Aerothermoelastic fluid–structure interaction (FSI) is a crucial problem in the design of supersonic and hypersonic vehicles, but modeling capabilities are in many cases quite limited. Insufficient treatment of FSI can limit design options or lead to damage or loss of vehicles. To improve understanding of such problems, we conducted FSI experiments with thin panels in hypersonic flow in the hypersonic wind tunnel H2K at DLR, Cologne, where both thermal and pressure-driven effects can be observed. Both cases with and without turbulent shock-wave/boundary-layer interaction (SWBLI) were considered. We obtained severe dynamic effects which led to the failure of the thinner panel. The results show a strong dependency of the dynamics of the coupled system on small temperature changes. Furthermore, we demonstrated that a large incident shock angle facilitates flutter in cases where it would not occur without incident shock. Detailed reference experiments regarding aerothermal heating, wall pressure and dynamic properties of the flow field were conducted using a rigid structure. This extends the very limited experimental data base on FSI in hypersonic flow serving as reference for modeling and preparation of new experiments.

1. Introduction

Understanding aerothermoelastic fluid–structure interaction (FSI) is crucial for the reliable design and life-time prediction of weight-optimized super- and hypersonic vehicle structures. Failure to appropriately address these issues can render design solutions impossible or lead to structural failures on flight vehicles [1–4].

The behavior of such a structure depends on a number of factors:

- The mechanical behavior of a structure depends on its mass, stiffness and damping, which has to be considered in conjunction with mounting and support structure.
- For high-speed vehicles, typically the thermal state of the structure is of central importance. The thermal state results from the thermal properties of the structure and from heat transfer to and from the flow field as well as the internal substructure [5]. This in turn affects the properties of the structure, which can result in changed stiffness and deformation which alters the dynamic behavior [6] and heat transfer [7].
- Suitable combinations of dynamic pressure, panel mass and stiffness can lead to panel flutter [8]. Panel flutter is strongly dependent on in-plane loading that can be connected to the thermal state of the structure or mechanical loads from the vehicle (e.g. [9]), that can both facilitate or inhibit panel dynamics. It also occurs for cases with incident shock, which has been shown to lower the required dynamic pressure for the onset of flutter in some cases [10]. Furthermore, both cases are influenced by the state of the boundary layer or SWBLI [11,12].

* Corresponding author.
E-mail address: dennis.daub@dlr.de (D. Daub).

https://doi.org/10.1016/j.jsv.2021.116714
Received 6 January 2021; Received in revised form 26 July 2021; Accepted 15 December 2021
Available online 5 January 2022

- A buckled structure can have more than one equilibrium position. In such cases, external loading can lead to a dynamic change between these states referred to as snap-through [13,14], which can alter the flow field, heat transfer and dynamic properties of the structure.
- Turbulence and SWBLI impose dynamic loads on the structure [15–17]. Furthermore, the state of the boundary layer or SWBLI has a large impact on heat transfer (e.g. [18–20]) and thus again the thermal state of the structure. In turn, the thermal state of the structure as well as static and dynamic deformation influence the behavior of the flow field [21–23].

Considering these processes, it becomes obvious that the behavior of the structure can be strongly path-dependent as demonstrated, for example, in [24]. These processes pose a complex challenge for the design of control surfaces, inlets and internal flow paths, nozzles but also for the surface structure of a vehicle, e.g. a reentry vehicle with a metallic thermal protection system [25,26]. Potentially opposing requirements arise if a broad range of flight conditions needs to be covered (e.g. large dynamic pressures and large heat loads occurring during different parts of the trajectory). Also, it is not necessarily apparent which combinations of loads and conditions of the structure can be considered worst cases, e.g. the combination of maximum heating and maximum dynamic pressure may well not be the worst case in terms of structural dynamics as heating may both inhibit or enable dynamic behavior of the structure.

Suitable modeling needs to be available that is both reliable and feasible in terms of computational resources. Wind tunnel experiments play an important role for validation data [27] and design especially in areas of complex interaction between the various discussed mechanisms. The present effort based within the Collaborative Research Center “Fundamental Technologies for the Development of Future Space-Transport-System Components under High Thermal and Mechanical Loads” (SFB TRR40) [28] of the German Research Foundation (DFG) aims at making a contribution in this area by conducting experimental studies of such fluid–structure coupled problems to help understand the fundamental processes and gain experience with structures under such conditions as well as providing validation or reference data for numerical simulations.

1.1. Previous work

1.1.1. Documented examples of FSI on flight vehicles

Examples of structural damage on flight vehicles are documented for the X-15. Melting damage due to enhanced heating near incident shocks was reported in [1] as well as thermal buckling near the wing leading edges [29]. Fatigue cracks were found on surface panels due to flutter occurring in flight, which was also reproduced in wind tunnel tests [2].

An Ariane 5 was lost due to insufficient load definition in the nozzle area resulting in the rapid disassembly of the main engine nozzle including buckling of cooling channels that define the shape of the nozzle contour [3,4].

It is also interesting to look at the development of the SR-71, for which, to the authors’ knowledge, no FSI related failures were reported. In the development phase, extensive thermomechanical testing was conducted, some of it even using full size vehicles [30,31]. The lower fuselage of the retired vehicles shows large plastic deformation [13].

Structural dynamics measurements of interstage adapters from three flights of Atlas-Centaur were reported in [32]. It was concluded that probably no panel flutter occurred and that the “high degree of skin oscillations” observed during these flights resulted from aerodynamic excitation. In [33], even a cryogenic tank was included in a wind tunnel flutter investigation to assure suitable boundary conditions.

Similarly, significant surface pressure fluctuations at lift-off and from the transonic well into the supersonic part of the trajectory of the first flights of the Saturn V were reported in [34]. Surface panels had been subjected to full scale wind tunnel tests where flutter was obtained for some conditions inside the flight envelope. Compressive loading as it would be imposed from the full vehicle was also considered [9,35].

1.1.2. Thermal effects

Heat transfer in a boundary layer has been thoroughly investigated for decades [18]. The possibly most challenging aspect troubling high-speed vehicles is the large difference in heat transfer between a laminar and a turbulent boundary layer, because the transition from laminar to turbulent is still not reliably predictable. Additionally, this process can locally enhance heat transfer beyond the level of a turbulent boundary layer [20]. A further complication occurs in cases with SWBLI, which can drastically enhance heat-transfer. SWBLI is in itself challenging to predict regarding its intrinsic properties but also strongly depends on the state of the incoming boundary layer [17,20]. At sufficiently high temperatures, effects such as chemical non-equilibrium come into play and catalytic effects on the wall might need to be considered [36]. Thermally coupled hypersonic FSI cases were considered in [37,38] where heating of a rigid structure in a high-temperature hypersonic flow environment in an arc-heated hypersonic wind tunnel was investigated and compared to thermally coupled simulations. The effect of similar flow conditions on a thin metallic panel showing significant thermal buckling including plastic effects with local increase in heat transfer due to the deformation of the structure was experimentally and numerically investigated in [39–42]. These studies, along with numerical investigations in [7,43–45], demonstrate the strong interdependence of heat transfer and structural deformation that makes coupled treatment of these problems inevitable for reliable predictions of temperature and deformation of the structure. An interesting complement to these studies, however, without flow field, is found in [46], where the thermal buckling behavior of similar structures was investigated experimentally, while localized heating was also considered.

1.1.3. Flutter

Flutter is well understood with regards to its onset for panel configurations [8]. In [11,47], important contributions were made on the effect of cavities underneath a panel and damping effects stemming from the boundary layer. The influence of in-plane loads obtained from aerodynamic heating of panels was studied experimentally in [48] and theoretically in [49]. In these experiments, panels were heated by the airflow, leading to buckling. In most cases, flutter occurred before buckling of the structure and subsided eventually because of the stiffening of the structure due to buckling, however, no full time-resolved data set was included. Similar results were also reported in [6]. In most other studies, the observations were limited to obtaining the conditions for flutter onset. A rare exception is the study in [50] that was specifically aimed at measuring flutter dynamics. It was found that in-plane compressive loads could reduce the dynamic pressure required for flutter onset to about a quarter of the value without such loads, whereas even a small rise in pressure differential significantly stiffened the panel. Thermal effects were not considered and compressive loads were applied by the experimental setup. However, heating would induce in-plane stresses in a similar way.

The influence of an incident shock on panel flutter was numerically investigated in [10,12] showing that the dynamic pressure required for flutter onset could be strongly reduced for such configurations with a strong shock, while a weak shock could even suppress panel flutter by stiffening the structure through added deformation.

The only published case known to the authors with full data not only on the onset but also on the panel dynamics during flutter with and without shock generator including thermal effects was reported in [13]. The temperature dependent behavior in the case without shock generator was studied in [51] using a low-fidelity simulation, which yielded very good agreement considering the limitations of the approach.

1.1.4. Snap-through

A buckled panel may have several equilibrium positions. Aerodynamic loads can cause a dynamic change between these. Reference experiments without flow field were conducted in [14,46,52]. In configurations with airflow, such behavior was observed in [13,41]. This behavior can depend strongly on thermal or vehicle-induced in-plane loads as well as pressure dynamics or excitation from the vehicle [24].

1.1.5. Turbulent effects and SWBLI

A notable example of the actual loads in a relevant environment was provided by [15], who measured boundary layer noise on X-15 on various locations and parts of the trajectory, reporting pressure dynamics of up to 150 db. Early ground experiments were conducted in [16,53,54] where the response of wall panels to attached or separated boundary layers was studied, showing that the presence of SWBLI can significantly increase panel dynamics compared to cases with an undisturbed boundary layer. Besides thermal aspects, the most striking feature of SWBLI is that it can produce low-frequency pressure oscillations in the order of about 100 – 1000 Hz [55], which is in a range relevant to vehicle structures. The effect of a turbulent SWBLI with large separation was studied in [38,56,57] showing excitation linked to the dynamics of the flow separation and also a feedback of the panel oscillations into the flow field detectable in high-speed Schlieren recordings and downstream pressure measurements. Furthermore, a coupled simulation including a LES flow field was conducted in [58]. Due to the short run time, the effect of the intrinsic SWBLI unsteadiness on the structure could not be analyzed sufficiently. However, a detailed comparison of the flow field for a rigid reference case was conducted, showing good agreement on the SWBLI pressure dynamics [59]. A similar configuration was also used in [13]. For this case, differences between experiment and simulation were observed that were assumed to be caused by the SWBLI dynamics not included in the modeling [60,61]. It was shown in [62] that excitation of some panel modes was stronger in presence of the SWBLI. A ramp configuration was used in [63] to induce SWBLI at the downstream end of a panel. It was found that the size of the separation changes the frequencies occurring in the observed panel dynamics. Furthermore, a feedback of the panel into the flow field was found as also reported in [13,38] for incident shock configurations.

An interesting example of the interaction of turbulent flow and structure was provided in [64] where a compliant rubber insert was used to reduce SWBLI dynamics. It was suggested in [65] that a turbulent boundary layer can have both a stabilizing or destabilizing effect on structural dynamics. A numerical study in [21] showed another intricate way in which structural dynamics can feed back into the flow field. For a configuration with an elastic panel, it was demonstrated that this configuration could actually promote boundary layer transition by conducting a fluid–structure coupled simulation using direct numerical simulation (DNS) for the flow field. Also, it was shown in [66] that intermittent turbulent spots can be used to excite a structure with structural responses, which greatly exceeded those with a laminar boundary layer.

1.2. Scope of the present work

The scope of the present work is the study of aerothermoelastic FSI in hypersonic flow with both temperature and pressure-driven effects with and without incident SWBLI. This is the only such study with incident shock in hypersonic flow, complementing previous work at lower Mach numbers [13,38,57]. Points of particular interest are:

- Structural dynamics of panel flutter in hypersonic flow, especially also the effect of the incident shock that was predicted to allow flutter in cases where it would not occur without incident shock [10,12]
- Effects of intrinsic low-frequency SWBLI dynamics, complementing observations in [38,60,61,63]
- Thermal effects that influence the dynamic behavior of the structure, leading to changes in the occurring frequencies as well as influencing the onset and stop of flutter, complementing results at lower Mach numbers [13] or obtained on a ramp configuration [63]

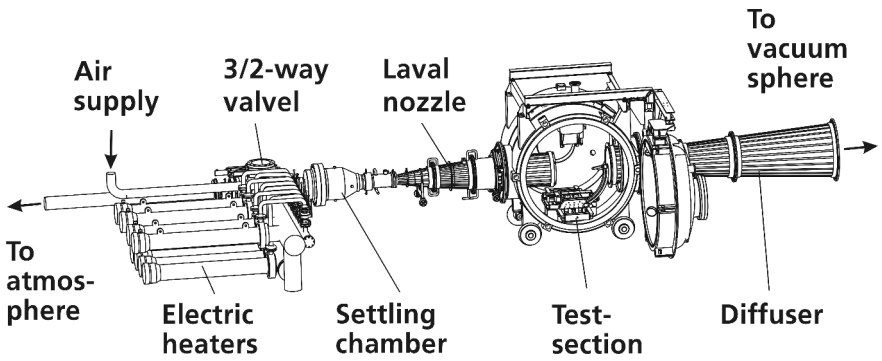

Fig. 1. Hypersonic blow-down wind tunnel H2K at DLR, Cologne.

Table 1
Nominal flow conditions.

M	p_0	T_0	p_∞	T_∞	u_∞	Re_∞
5.33	1250 kPa	390 K	1628 Pa	58 K	816 m/s	$19.3 \cdot 10^6$/m

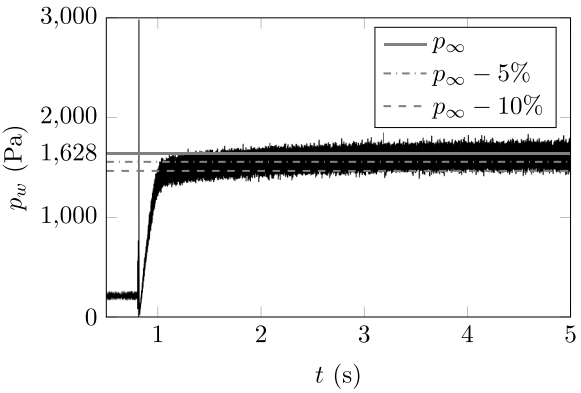

Fig. 2. Wall pressure (p_w) during wind tunnel start.

2. Experiment

2.1. Wind tunnel H2K

The experiments were performed in the hypersonic wind tunnel H2K at DLR, Cologne (Fig. 1) [67]. H2K is a blow-down facility with a free jet test section. Resistance heaters are used to adjust the total temperature. The nozzle can be exchanged to vary the Mach number. The nozzle exit diameter is 600 mm. The turbulent intensity in the undisturbed inflow was measured using Laser-2-Focus velocimetry [38] and found to be about 1%. Maximum test time is about 30 s depending on flow conditions.

Flow conditions (Table 1) were chosen to obtain the maximum Reynolds number available at a Mach number of 5.33. The flow conditions include a correction depending on the Reynolds number, which accounts for the boundary layer thickness in the nozzle [67]. Free stream conditions were calculated from the measured total conditions using isentropic equations [68]. Viscosity was calculated using a power-law approximation for low temperatures [36]. The molar gas constant was used according to [69] and the mean molecular weight of dry air was used as stated in [36].

Total pressure (p_0) was measured using a piezoresistive pressure sensor GE UNIK 5000 with an uncertainty of 0.04% of 5 MPa full scale range. Total temperature (T_0) was measured in the settling chamber (Fig. 1) using a Type K thermocouple with an uncertainty of 0.4% of the measured temperature. Small variations in total pressure and temperature occur between the wind tunnel runs. The runs presented were within 1% of nominal p_0 and 1.3% of nominal T_0 unless otherwise noted.

Before the wind tunnel run is started, the airflow is directed through the heaters and into an exhaust pipe. Only once nominal conditions are reached, the flow is redirected into the nozzle using the valve shown in Fig. 1. In this way, the flow in the test section is close to nominal conditions in about 0.2 s (Fig. 2).

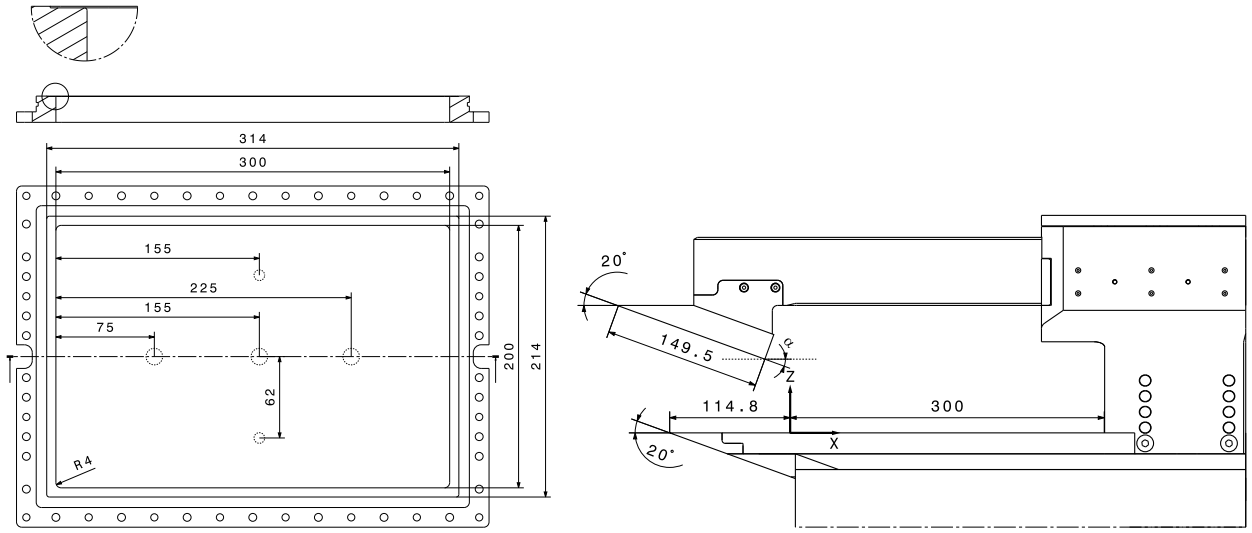

(a) Frame with elastic panel, sensor positions (dashed circles)

(b) Wind tunnel model, shock generator angle (α)

Fig. 3. Model geometry (all measures in mm).

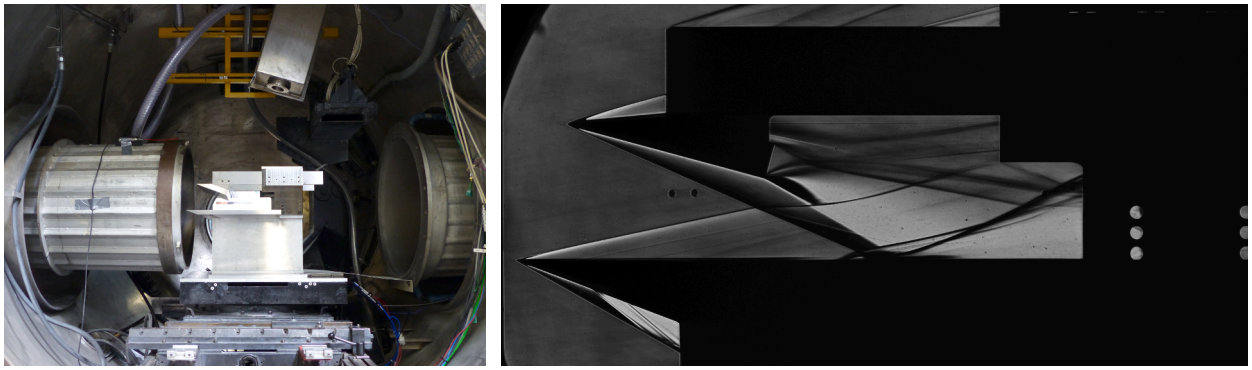

(a) Side view of the wind tunnel model in the H2K test section

(b) Example Schlieren image

Fig. 4. Setup.

2.2. Wind tunnel model

2.2.1. Configuration

The elastic panel/frame assembly was mounted in a flat plate with a sharp leading edge inside the free jet test section of H2K (Fig. 4). Thus, well defined boundary conditions on the flow side are established as a new boundary layer forms, originating from the leading edge of the model. Furthermore, there is no influence on the flow field from side walls. Fig. 4b shows a Schlieren image during a wind tunnel run to clarify the wind tunnel model configuration and basic properties of the flow field. The shock generator on top is removable and adjustable in height and angle towards the flow field as well as axial position in flow direction. For the present experiments, it was adjusted so that the nominal impingement point remains at the center of the exchangeable insert in the bottom wall (x = 150 mm). This wall always remains parallel to the direction of the undisturbed flow field. Both the shock generator and the lower wall have 20° leading edges. The elastic part of the exchangeable wall section begins 114.8 mm from the leading edge. The coordinate system is placed at this position with x facing in free stream flow direction (Fig. 3b). Fig. 3a shows the frame for flush mounting the elastic insert with a thickness of 0.3 mm. In this way, panels with a free surface area of 300 mm x

Table 2
Displacement sensor positions.

Sensor type	Position	x (mm)	y (mm)
CS5	Front	75	0
CS5	Center	155	0
CS5	Rear	225	0
CSH2FL	Left	155	62
CSH2FL	Right	155	−62

200 mm can be mounted. Panels with 0.3 mm and 0.7 mm nominal thickness made of stainless steel (1.4301) were manufactured. The thickness of the panels was found to be 0.307 mm and 0.687 mm. Total model width is 400 mm. The width of the shock generator is 390 mm.

2.2.2. Design of the elastic panel

Different options for manufacturing the elastic panels were considered. Machining the panel/frame assembly from a solid piece is beneficial due to the good connection of panel and frame [13], but manufacturing panels of the desired size and thickness was unsuccessful. Using adhesive to fix the panel to a frame is favorable because a high-precision panel can easily be obtained and its properties are not changed by the mounting procedure. The downside of this method is that the behavior of the adhesive, especially while undergoing temperature changes, would be challenging to model even if an adhesive sufficient for the desired temperature range could be found. Flush rivets as used in [38] require a certain panel thickness and are thus not suitable for very thin panels either. Considering these aspects, laser welding was chosen to manufacture the present set of panels because it can withstand thermal loads, and a high-precision laser-cut panel can be used. The laser was set to minimal power to obtain a good connection while keeping the induced stresses at a minimum. As the weld is warm on all sides during manufacturing and cools down afterward, this procedure leads to a somewhat prestressed panel.

2.3. Instrumentation and data processing

2.3.1. Rigid reference panel

A rigid polyether ether ketone (PEEK) panel of 20 mm thickness, which could be inserted in place of the elastic panel, was used for reference measurements. It was outfitted with Pressure Systems Inc. (PSI) 1615B-TL pressure scanners connected to pressure ports to assess the static pressure distribution on the panel. Uncertainty for these sensors is 0.05% of the 100 kPa range. PCB 132A31 (with PCB 482C05 conditioner modules) were used for high-frequency pressure measurements. These sensors are designed for time-of-arrival measurements but have been shown to be useful to measure high-frequency pressure fluctuations in transitional and turbulent boundary layers (see [19] for a detailed discussion).

The surface temperature was recorded using an infrared camera InfraTec ImageIR 8380 (640 × 512 pixels, 2 – 5.7 μm) with a maximum frame rate of 100 Hz. The measurement uncertainty given by InfraTec for measurements below 372.15 K is 1 K. The geometrical properties of the system were calibrated using a GOM CP 20 reference object. The image position was thus corrected using the in-house tool ROBOT [70]. Heat fluxes into the wall were calculated using the in-house tool VisualHeatflow [71], assuming one-dimensional heat flow. The lower wall of the rigid panel facing into the cavity was assumed to be adiabatic. For comparison, Stanton numbers for a laminar and turbulent boundary layer were computed using the correlations given by Korkegi [72]. Prandtl number and recovery factor were chosen according to [36].

2.3.2. Elastic panel

The elastic panels were instrumented with several non-intrusive distance sensors placed underneath the panel. Three capacitive distance sensors CS5 and two CSH2FL by Micro-Epsilon were used with Micro-Epsilon capaNCDT 6350 amplifiers enabling measurements at 50 kHz (−3 db). The maximum operating temperature of the sensors is 200° C with a temperature sensitivity of −160 nm/K, thus no relevant effect of the sensor temperature on the distance measurements is expected. The non-linearity of the sensors is smaller than 12 μm for the CSH2FL used with 4 mm range and smaller than 15 μm for the CS5 with 5 mm range. For the runs where measurements exceeded 5 mm, the range of the CS5 sensors was doubled, also doubling the non-linearity estimate. The sensor positions are listed in Table 2. The power spectral density (PSD) of the measured deformation was calculated following Welch's method [73], using Hann windows, a block length of 10 000 samples and an overlap of 0.5 resulting in a frequency resolution of 5 Hz. For the spectrograms, the PSD was averaged for 5 blocks with an overlap of 0.6, resulting in a time step of 0.2 s.

Two GE UNIK 5000 pressure sensors with 10 kPa and 20 kPa range were used to measure the pressure inside the cavity underneath the panel with an uncertainty of 0.4% of their respective range, allowing measurements at up to 5 kHz.

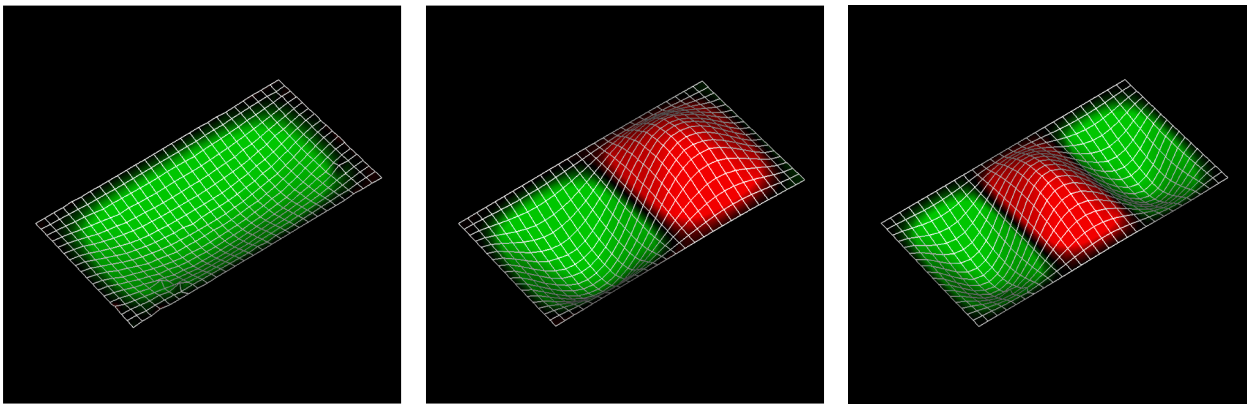

(a) 255 Hz (b) 341 Hz (c) 436 Hz

Fig. 5. Examples of measured modes of the 0.7 mm panel without flow (amplitudes not to scale).

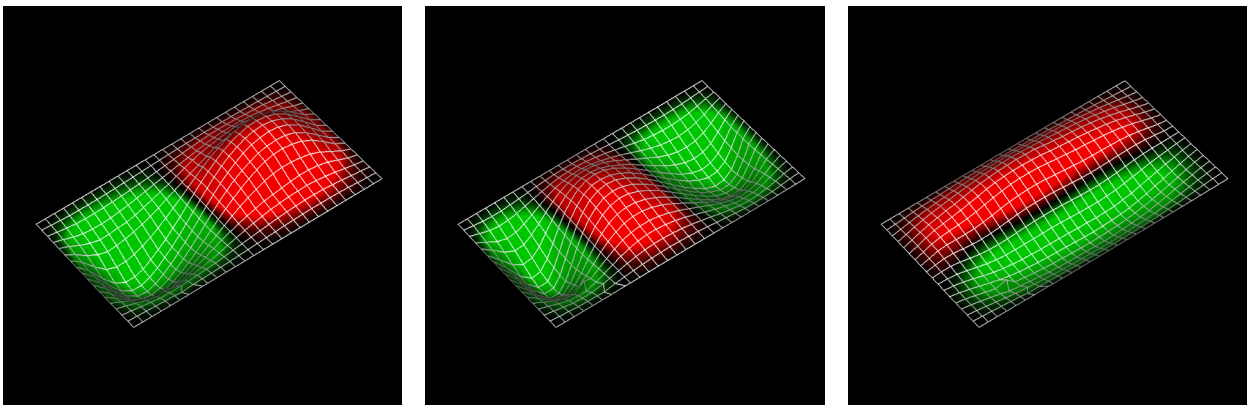

(a) 305 Hz (b) 363 Hz (c) 548 Hz

Fig. 6. Examples of measured modes of the 0.3 mm panel without flow (amplitudes not to scale).

2.3.3. Flow field

Special attention was given to the Schlieren optical system. Previously, a coincident Schlieren system was used at H2K. This system was designed for maximum sensitivity but has some drawbacks regarding sharpness of the images and two-dimensional configurations. Thus, the system was replaced by a newly built Z-type setup with 600 mm diameter mirrors with 6 m focal length. To allow short duration imaging, the FASTCAM SA-X2 high-speed camera was outfitted with a 290 ns shutter. Due to the free jet test section of H2K, the present setup will not suffer from a distortion of the flow field caused by the wind tunnel walls, which obstructs the view of the test section center in similar setups [57,74], complicating the analysis of the flow field. High-speed videos were recorded in shadowgraph configuration (without knife-edge). The frame rate was set to 10 kHz to resolve effects of structural dynamics on the flow field as well as low-frequency dynamics of the SWBLI. The analysis was conducted similarly to [75,76], calculating the PSD of the intensity for each pixel again using Welch's method with Hann windows, a block length of 1000 samples and an overlap of 0.5, resulting in a frequency resolution of 10 Hz.

2.4. Properties of the elastic panel

2.4.1. Dynamic properties

Prior to the wind tunnel runs, the properties of the elastic panel were investigated using an automatic impact hammer Maul-Theet vlimpact-60 equipped with a force sensor located at $x = 240$ mm; $y = 45$ mm and a Maul-Theet ScanSet. This system is equipped with a laser Doppler velocimeter OptiMet Nova that allows to measure surface velocity at multiple locations to obtain eigenfrequencies of the panel and respective mode shapes. The results are shown in Figs. 5, 6. In the latter case, it appears that the first eigenmode was not sufficiently excited for detection. Furthermore, in addition to the described pre-stress of the panels from the welding procedure, we found an influence of the panel mounting on the eigenfrequencies of the panel.

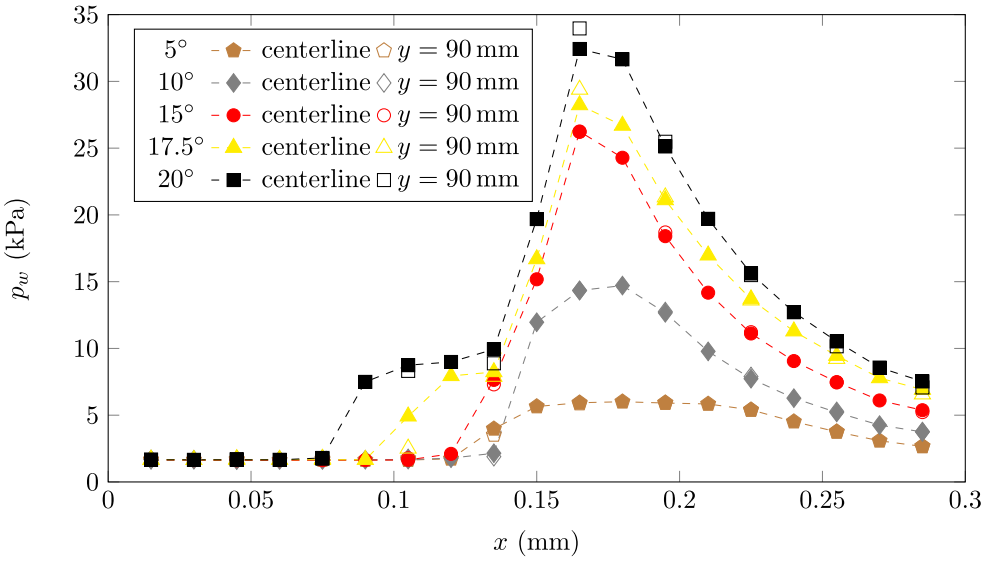

Fig. 7. Time-averaged wall pressure on the rigid insert for various shock generator angles.

An ANSYS finite element method (FEM) model was set up to support this assumption and analysis of the measured panel dynamics. The edges of the panel were considered clamped and subjected to small in-plane displacement to adjust the pre-stress. A density of 7900 kg/m^3 and an elastic modulus of 200 GPa were used [77]. The result was compared to the measured eigenfrequencies of the panel after the final mounting in the wind tunnel. A discussion and results are included in the discussion of the experimental results. Calibrating a structural model with measured results commonly appears to be necessary for similar setups [13,51].

2.4.2. Back pressure and cavity effect

In addition to the wall pressure on the side of the panel that is exposed to the flow, the pressure underneath the panel is an important boundary condition. A pressure difference across the panel leads to deformation and induces stresses that reduce structural dynamics (e.g. [56]). To avoid this, we set the back pressure to the average wall pressure obtained from the reference experiments with the rigid insert. The pressure was set before wind tunnel start-up and the cavity underneath the panel remained sealed throughout the run. Small leakage occurred most likely along the cabling of the instrumentation in the cavity. This could not fully be avoided, but appeared to have no detrimental effect on the experimental results. A discussion and cavity pressure measurements for all runs are included with the experimental results. Furthermore, the cavity itself can have an influence on the panel dynamics [47]. A calculation for a cavity of the same size for various pressure levels is provided in [38], showing that no significant effects are expected for the present configuration because of the low cavity pressure. The volume of the cavity is 0.0022 m^3.

3. Experimental results

3.1. Rigid panel

3.1.1. Wall pressure

Fig. 7 shows time-averaged wall pressure measurements on the rigid wall for various shock generator angles on and off the centerline. As expected, the maximum pressure rises with increased shock generator angle. For the largest shock generator angles, the initial pressure rise takes place considerably upstream of the nominal impingement position in the center of the panel due to the occurring flow separation. The second distinct pressure rise in these cases is caused by the reattachment shock on the downstream side of the separated area. This flow structure can also be observed in the shadowgraph images (Fig. 8) as well as in the resulting heating of the wall (Figs. 11 and 13). In lateral direction, the pressure measurements show good agreement, confirming that the flow field is nearly two-dimensional in the area on the insert.

The results of the measurements using the PCB 132A31 high-speed pressure sensors have been moved to the appendix as they are not considered central for the present investigation. However, they support the diagnosis regarding the state of the boundary layer and show significant dynamics in the SWBLI area at frequencies beyond the scope of the present investigation.

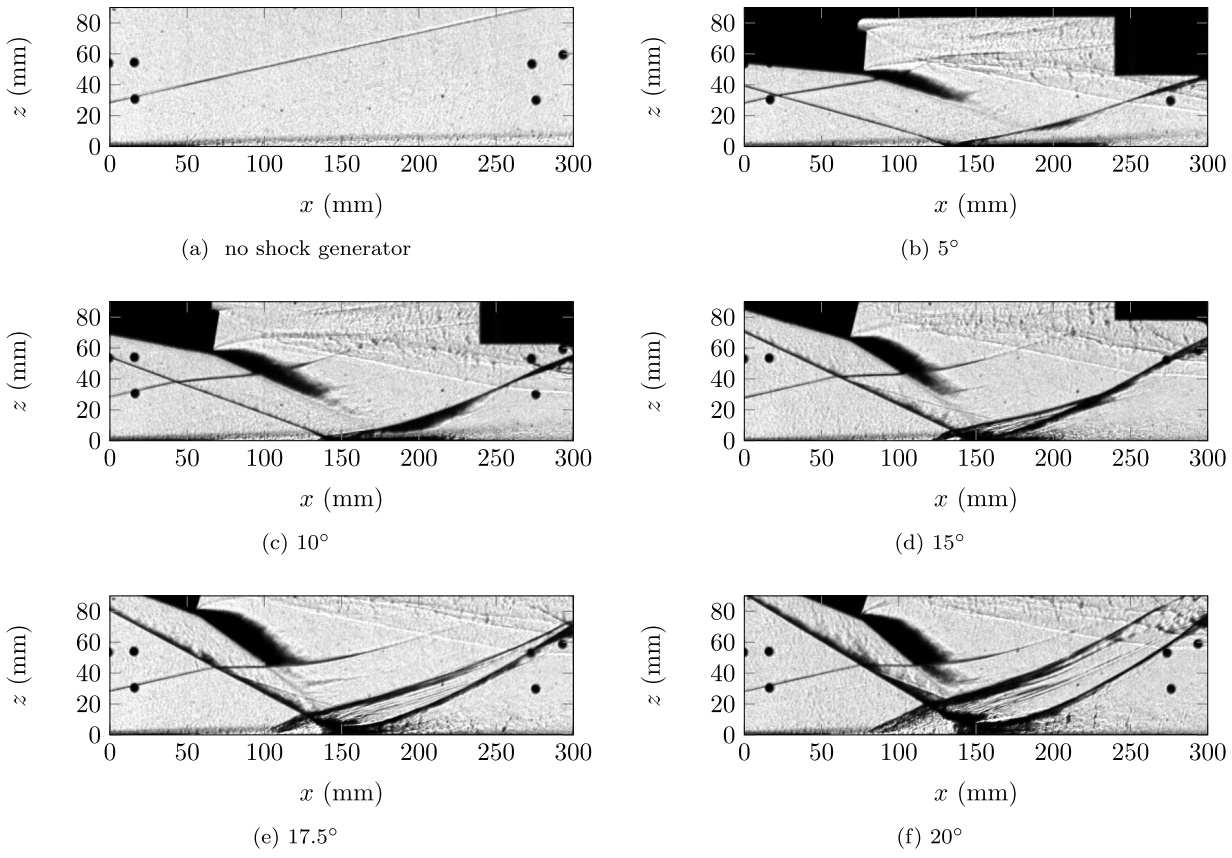

Fig. 8. Shadowgraph images at various shock generator angles on a rigid wall.

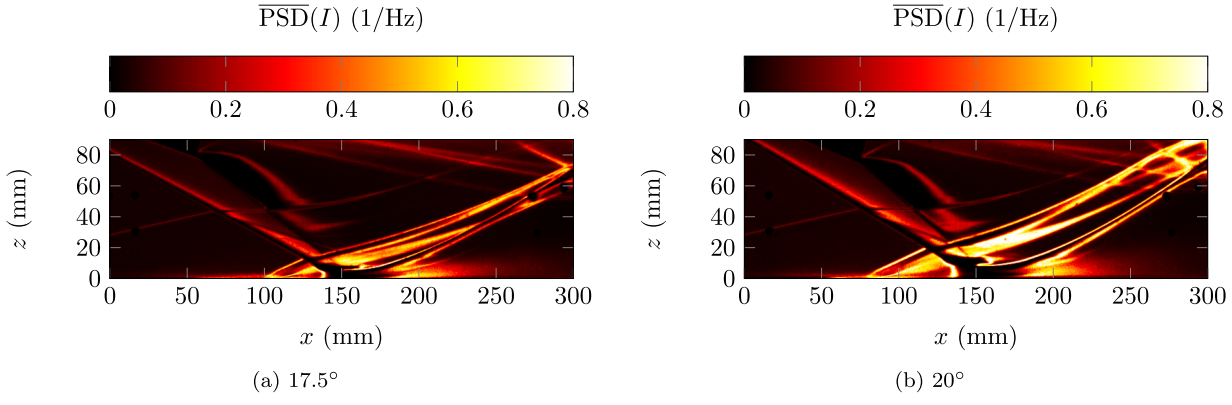

Fig. 9. Mean PSD of the gray values of the high-speed shadowgraph videos.

3.1.2. Shadowgraph

Figs. 8a–8f show frames from the recorded high-speed shadowgraph videos for the case with rigid wall insert. In Fig. 8a, some turbulent structures in the boundary layer are visible. The apparent change near $x = 50$ mm is caused by the laminar–turbulent transition of the boundary layer taking place in this area. In Figs. 8b, 8c, for cases with low shock generator angle, no significant flow separation is caused by the incident shock. For the cases with larger shock generator angle, it grows considerably larger with increasing shock generator angle (Figs. 8d, 8f), which is consistent with the observed wall pressure distribution (Fig. 7). Such flow fields with large separation typically exhibit significant dynamics, including relatively low-frequency dynamics of the separation shock on the wall [55,59]. We used the high-speed shadowgraph recordings to investigate these dynamics. Figs. 9a–9b show the

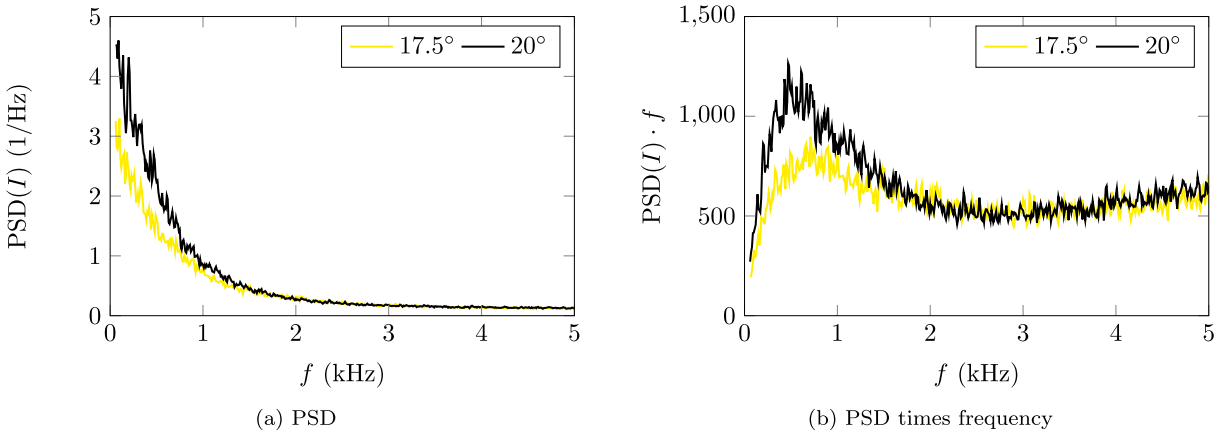

(a) PSD (b) PSD times frequency

Fig. 10. PSD of separation shock dynamics for 17.5° and 20° shock generator angle on a rigid wall.

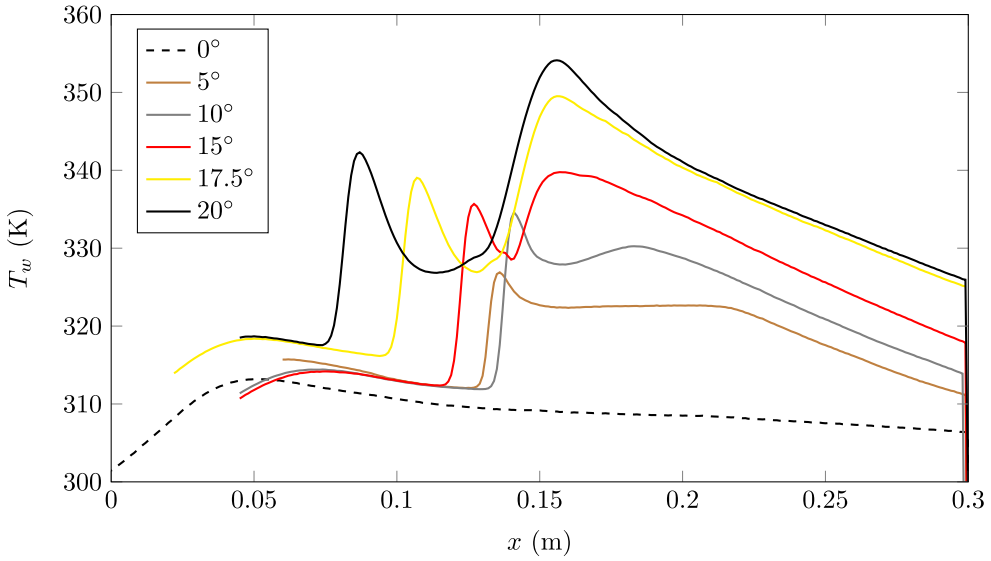

Fig. 11. Wall temperature after 10 s on the rigid panel for various shock generator angles.

mean PSD of the gray value of each pixel of these videos, revealing significant dynamics throughout the separation region. The comparison between both cases shows that dynamics considerably increase with an increase in shock generator angle and resulting size of the separation. Similar observations using this method were made in [76] for flow separation upstream of a ramp that has partly similar properties. This method only gives qualitative information regarding the spatial distribution of the SWBLI dynamics and only works for such structures that show up in the recorded images.

Fig. 10 shows spectra obtained at the separation shock where significant low-frequency dynamics can be observed, yielding a local maximum below 1 kHz in frequency-multiplied form, which is in the same order of magnitude as the eigenfrequencies of the elastic inserts. This behavior is qualitatively in line with previous observations from experiments and simulations, e.g. [59].

3.1.3. Temperature

Fig. 11 shows the wall temperature of the rigid PEEK insert after 10 s for various shock generator angles and without shock generator. For the runs with 17.5° and 20° shock generator angle, the inflow total temperature was about 5 K above the nominal value, leading to the slightly higher observed wall temperature. The rise in wall temperature between $x = 0$ mm and $x = 50$ mm is caused by the laminar–turbulent transition of the boundary layer taking place in this area (see also Fig. 8a). The view of this area on the wind tunnel model was partly blocked by the shock generator for the other cases. The slight shift of the transition

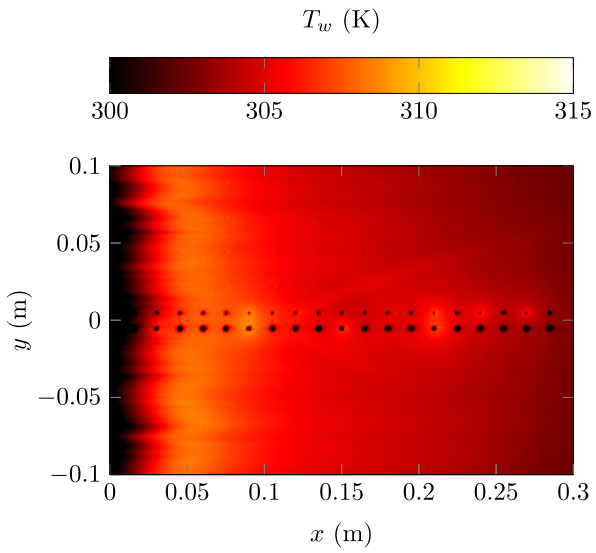

(a) Wall temperature without incident shock after 5 s

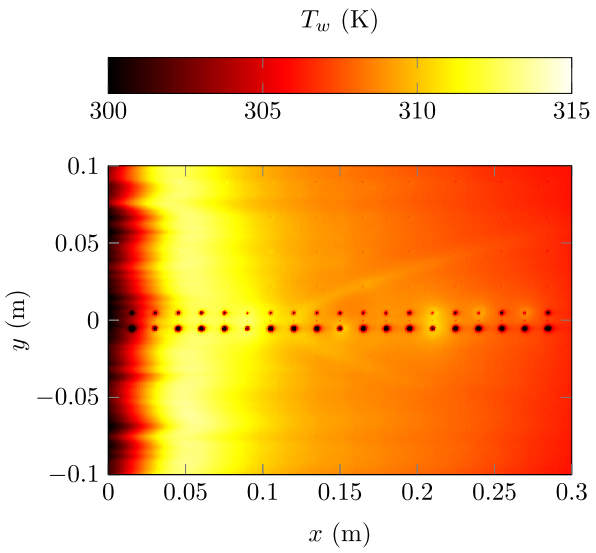

(b) Wall temperature without incident shock after 10 s

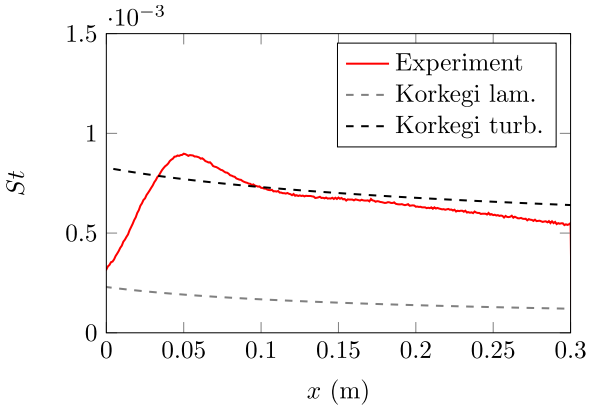

(c) Stanton number, comparison to correlation by Korkegi [72]

Fig. 12. Temperature distribution on a rigid wall without incident shock.

location is probably caused by some degradation of the sharp leading edge of the wind tunnel model throughout the experiments. For configurations with 15° shock generator angle or more, two distinct maxima appear that correspond to the locations of the separation and reattachment shocks (see also Figs. 7, 8). Fig. 12 shows the surface temperature distribution without shock generator. As in Fig. 11, the locally increased wall temperature due to the boundary layer transition is clearly visible and nearly constant in lateral direction. To further confirm the presence of a turbulent boundary layer on most of the insert, the heat flux into the wall was computed and compared to heat transfer correlations for laminar and turbulent boundary layers (Fig. 12c). This clearly indicates transition at the upstream end of the panel and a turbulent boundary layer on most of the panel. Agreement between the correlation and computed data is within a typical range (e.g. [19]). Fig. 13 shows the surface temperature for the runs with 17.5° and 20° shock generator angle. In the white area, the view is blocked by the shock generator. The temperature distribution very distinctly shows the locally increased wall temperature near separation and reattachment. The variation in x-position of the separation is caused by lateral flow in the separated area that cannot fully be avoided for a wind tunnel model of finite width (see also [78] for a surface oil flow visualization of a similar configuration). However, this does not have a significant effect on the measured wall pressure distribution in lateral direction (Fig. 7). The absence of changes in lateral direction of the second maximum attests to the good homogeneity of the incoming flow field as deviations in the Mach number would change the incident shock location.

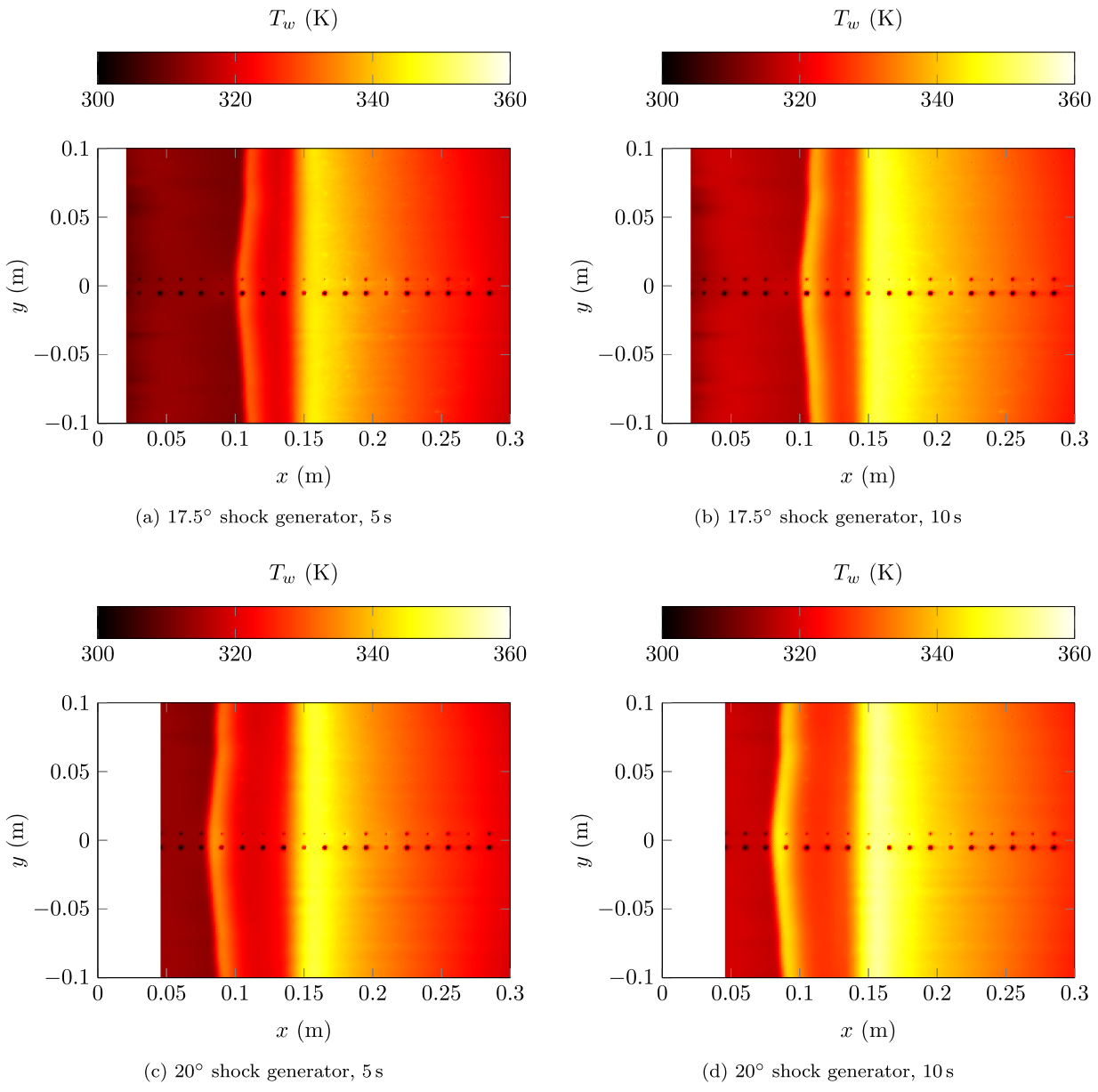

(a) 17.5° shock generator, 5 s

(b) 17.5° shock generator, 10 s

(c) 20° shock generator, 5 s

(d) 20° shock generator, 10 s

Fig. 13. Temperature distribution on a rigid wall with incident shock.

3.2. FSI

3.2.1. 0.7 mm panel

For all runs with an elastic panel, the back pressure underneath the panel was set to be equal to the average wall pressure on the undeformed wall. Because the test section is initially evacuated, the panel deforms towards the test section before flow start-up for all wind tunnel runs. Upon wind tunnel start-up, the panels quickly assume a neutral position for the cases without shock generator (Figs. 14a, 14b). For cases with shock generator, the panel directly enters a deformed state, with the upstream part of the panel bending into the flow and the downstream part away from the flow (e.g. Fig. 15a) caused by the uneven pressure distribution on the panel (Fig. 7). This behavior becomes more distinct with rising incident shock angle.

Several runs without shock generator were conducted before and after the cases with shock generator to obtain reference information on thermal and dynamic behavior and thus to assess potential changes in the behavior of the structure (Fig. 14b). As there appears to be an effect of the panel mounting on the prestress of the structure, the first second after flow start-up of the runs without shock generator was used to obtain spectra of the structural dynamics to check for changes between the runs and to serve as

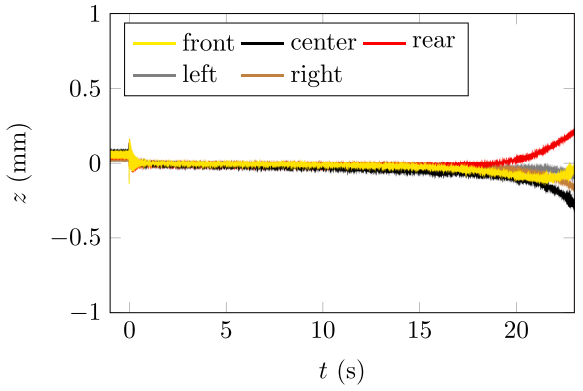

(a) Run 5 displacement

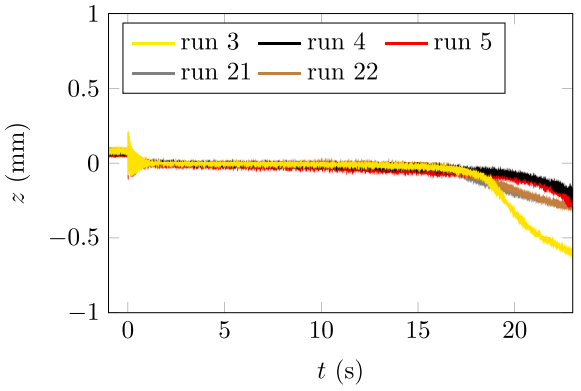

(b) Center sensor displacement for run 3−5, 21, 22

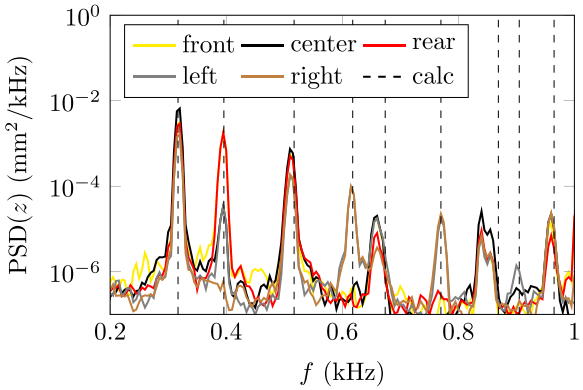

(c) Run 5 displacement PSD 0.5−1.5 s

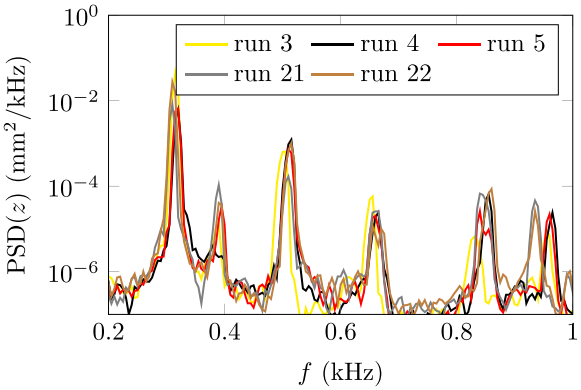

(d) Center sensor displacement PSD 0.5−1.5 s for run 3−5, 21, 22

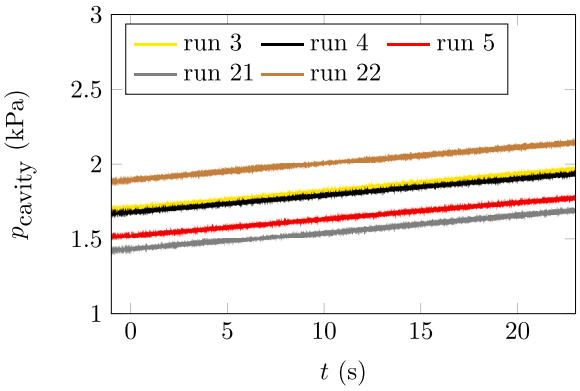

(e) Cavity pressure for runs 3−5, 21, 22

Fig. 14. Panel displacement for 0.7 mm panel without shock generator (p_0 during run 22 was 1.4% below the nominal value).

Table 3
Computed panel modes for the 0.7 mm panel (number of neutral lines in x;y-direction).

Panel modes (Hz)								
0;0	1;0	2;0	1;1	3;0	2;1	4;0	3;1	0;2
317	396	517	618	674	770	869	905	965

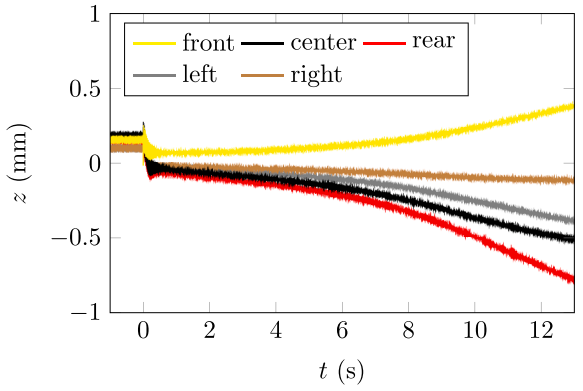

(a) Run 6 displacement, 5° shock generator

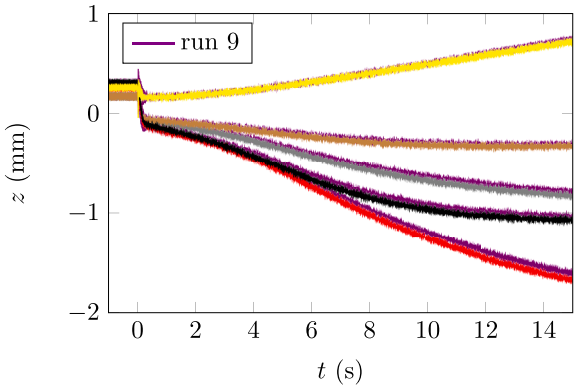

(b) Run 8, 9 displacement, 10° shock generator (Run 9 in background)

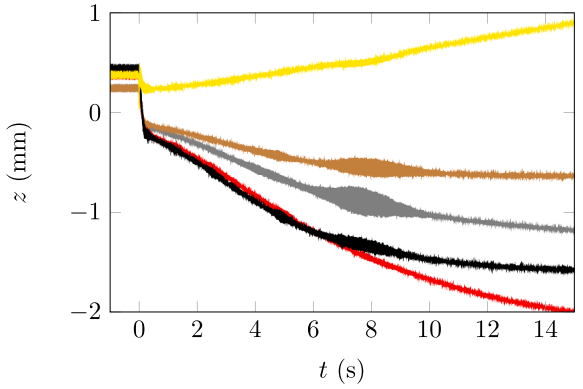

(c) Run 10 displacement, 15° shock generator

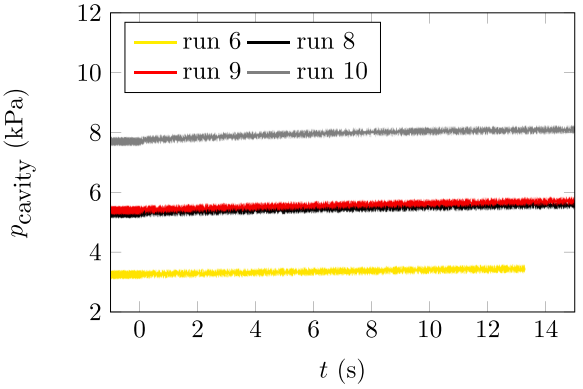

(d) Cavity pressure for runs 6, 8−10

Fig. 15. Panel displacement for 0.7 mm panel and various shock generator angles.

reference for modeling because at this time the panel has not yet heated up significantly. These spectra were compared to solutions generated with ANSYS (Table 3) that show good agreement for the lower modes if small in-plane stresses are applied to match the stresses that appear to have been induced by welding and mounting (Fig. 14c). Thus, the occurring frequencies are higher than in a non-prestressed case. Agreement between different runs is good with only small differences occurring at higher frequencies (Fig. 14d) after the runs with the maximum structural dynamics (Figs. 16, 18). Fig. 14e shows the backpressure underneath the panels. A small leakage into the cavity occurred most likely along the cabling of the deformation measurement instrumentation. This could not fully be avoided. To evaluate whether this has a significant effect on panel dynamics or deformation, a small variation of the cavitiy pressure in the same range as the change in pressure due to the leakage was investigated (Fig. 14e). No significant effect on static deformation (Fig. 14b) or panel dynamics (Fig. 14d) was found.

In the course of the wind tunnel runs without incident shock (Fig. 14a), the 0.7 mm panels remain at a neutral position and only start to buckle at about 17 s. The timing of the buckling onset shows good agreement between the runs, however, for the case without shock generator, some differences occur regarding the resulting deformation (Fig. 14b). With addition of the shock generator (Fig. 15a), buckling starts to occur earlier due to the increased heating (Fig. 11) and reaches larger amplitudes. This behavior becomes more distinct with further increases in shock generator angle (Figs. 15b, 15c). Fig. 15b contains two wind tunnel runs, demonstrating the very good repeatability between runs both regarding timing and amplitude of the occurring deformation. For reference, Fig. 15d shows the measured back pressure for the previous cases. In the run with 15° shock generator, somewhat increased structural dynamics occur at about 7 – 9 s (Fig. 15c) interestingly predominantly in the 0;1 mode. Generally, during the wind tunnel runs at constant flow conditions two main effects change the dynamic properties of the structure. As the structure is initially prestressed, heating and the following expansion reduce the stiffness of the structure. However, large panel deformation also following from the thermal expansion of the panel can substantially stiffen the structure. The previous run shows that the occurring structural dynamics depend on the specific state in the transient change of structural properties.

At 17.5° and 20° shock generator angle, we obtained significant structural dynamics (Figs. 16, 18). These runs were repeated to assess repeatability. For both cases, we obtained good agreement between the high-speed displacement signals (Figs. 16a, 16b, 18a,

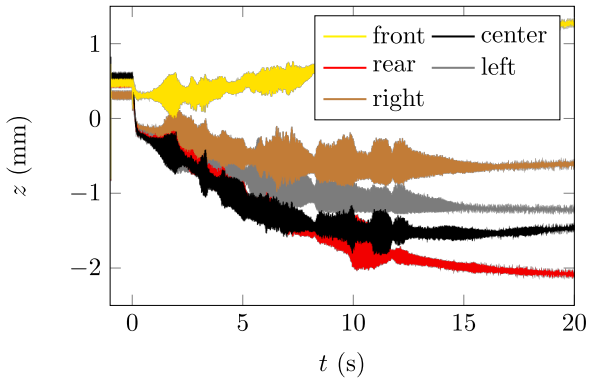

(a) Run 13 displacement

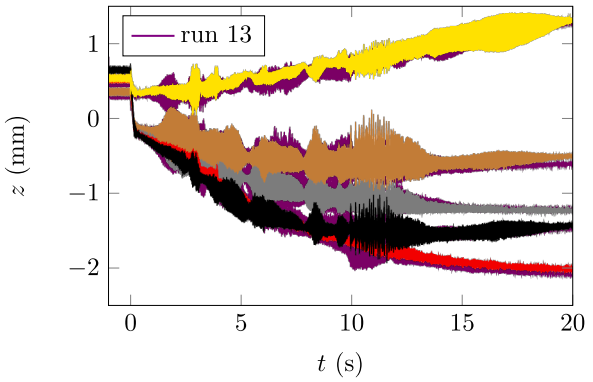

(b) Run 20 displacement (Run 13 in background)

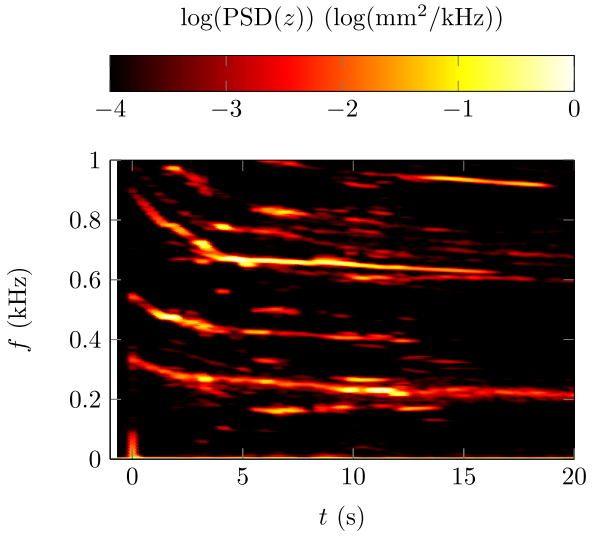

(c) Run 13 center displacement spectrogram

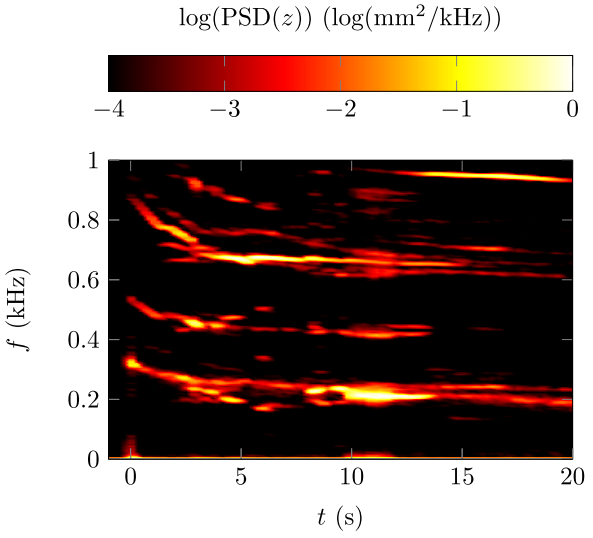

(d) Run 20 center displacement spectrogram

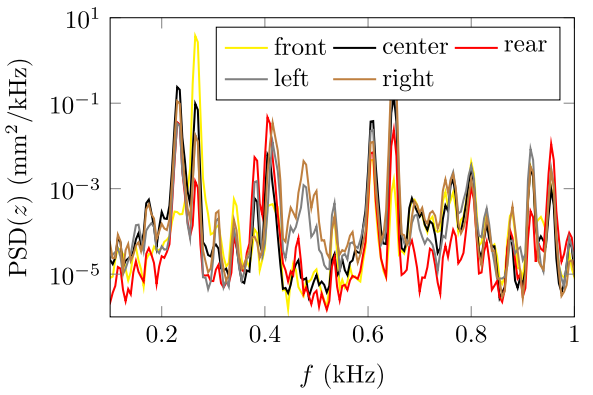

(e) Run 13 displacement PSD 10 – 11 s

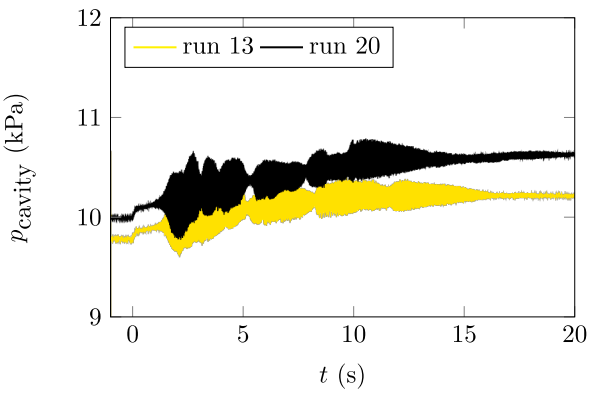

(f) Run 13, 20 cavity pressure

Fig. 16. Panel displacement for 0.7 mm panel and 17.5° shock generator.

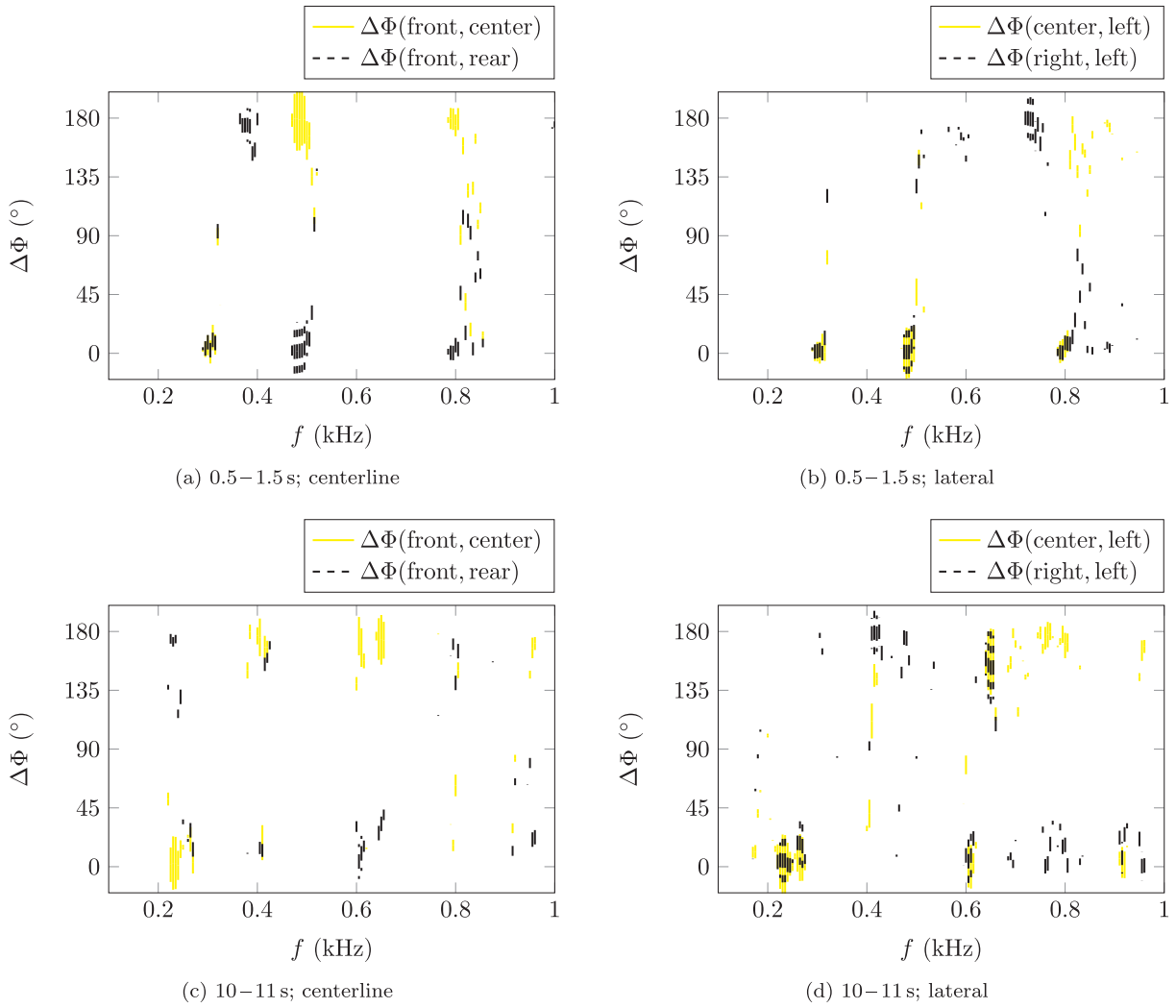

(a) 0.5 – 1.5 s; centerline

(b) 0.5 – 1.5 s; lateral

(c) 10 – 11 s; centerline

(d) 10 – 11 s; lateral

Fig. 17. Run 13 phase difference ($\Delta\Phi$) of the panel displacement for 0.7 mm panel and 17.5° shock generator.

18b) and the resulting spectrograms (Figs. 16c, 16d, 18c, 18d). Also note that run 13 was conducted before the 20° shock generator runs and run 20 afterward. The good agreement suggests that no significant damage to the structure was incurred.

For the cases with 17.5° shock generator (Figs. 16a, 16b), oscillations of the panel started shortly after start-up of the wind tunnel. A deformed shape with the upwind part bending into the flow and the downstream part away from the flow occurred immediately after start-up due to the pressure gradient from the SWBLI (Fig. 7). The deformation keeps increasing throughout most of the wind tunnel run as the panel heats up and buckles against its frame. At about 13 s, the buckling (and stiffening) of the panel leads to a drastic reduction in structural dynamics. For the 20° shock generator runs (Figs. 18a, 18b), the situation is similar with the most notable difference that the onset of the panel oscillations occurred immediately after start-up and reached greater amplitudes. As in the previous case, the buckling of the panel led to a strong reduction in panel dynamics.

The spectrograms (Figs. 16c, 16d, 18c, 18d) indicate that the panels were excited at various frequencies, presumably connected to modes with neutral lines in lateral direction since similar behavior is found in the off-centerline sensors (Figs. 16e, 18e). However, in the case with 17.5° shock generator, a mode with neutral line in flow direction was excited as well near 480 Hz (Fig. 16e). Increases in PSD for the off-centerline sensors at a similar frequency are also visible for the 20° shock generator case but nearly coincide with a larger peak at slightly lower frequency found at all sensor positions (Fig. 18e). The spectrograms for both cases show a distinct change in the occurring frequencies, especially during the first 3 – 4 s of the run when maximum heating and change in deformation take place.

Figs. 16f, 18f show the respective back pressure that was influenced by the panel dynamics. Furthermore, the pressure increase during the run was considerably larger than in the previous cases with lower shock generator angle. This is probably caused by the increased heating and compression of the enclosed air in the cavity. Both effects are expected to be in the same order of magnitude.

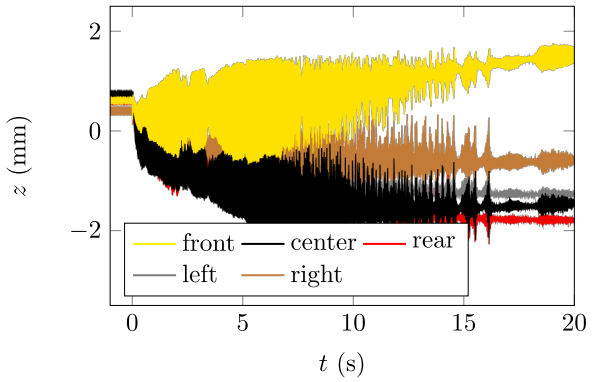

(a) Run 17 displacement

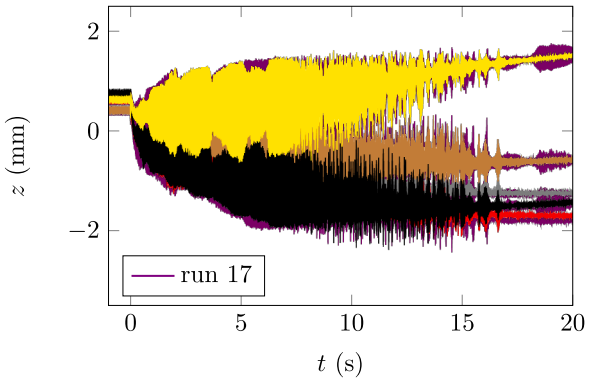

(b) Run 18 displacement (Run 17 in background)

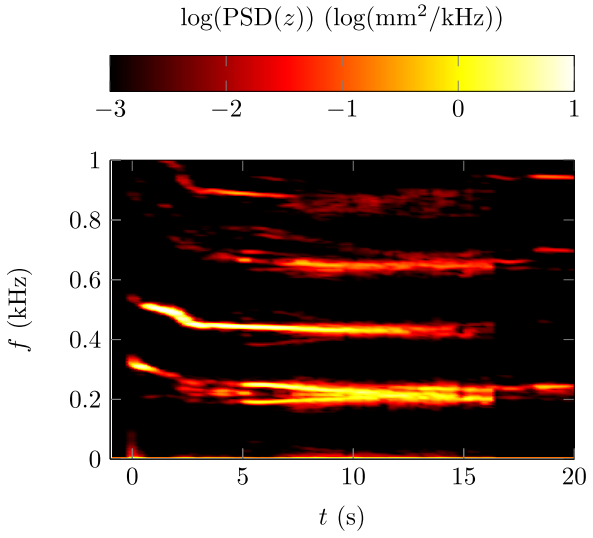

(c) Run 17 center displacement spectrogram

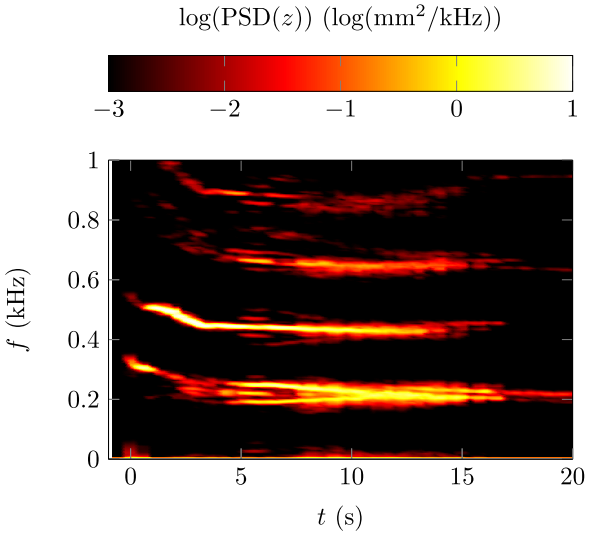

(d) Run 18 center displacement spectrogram

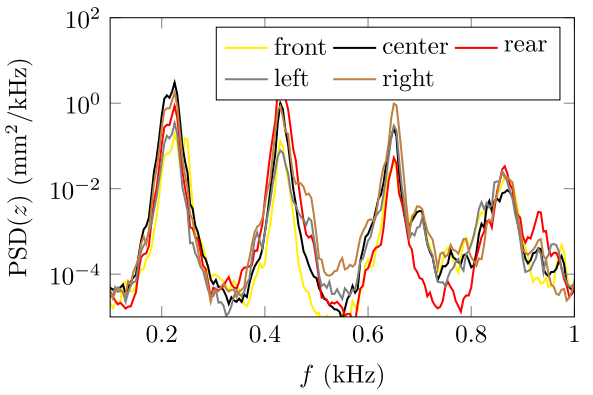

(e) Run 17 displacement PSD 10 – 11 s

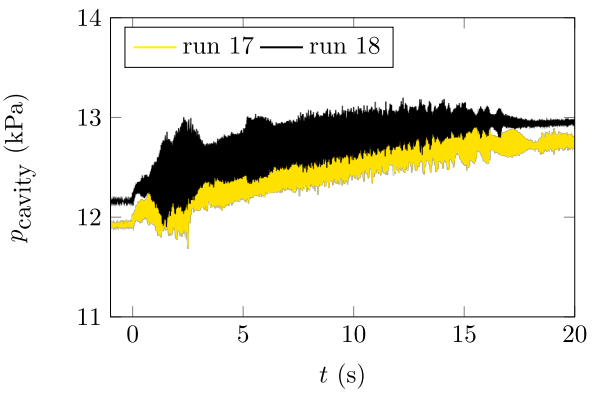

(f) Run 17, 18 cavity pressure

Fig. 18. Panel displacement for 0.7 mm panel and 20° shock generator.

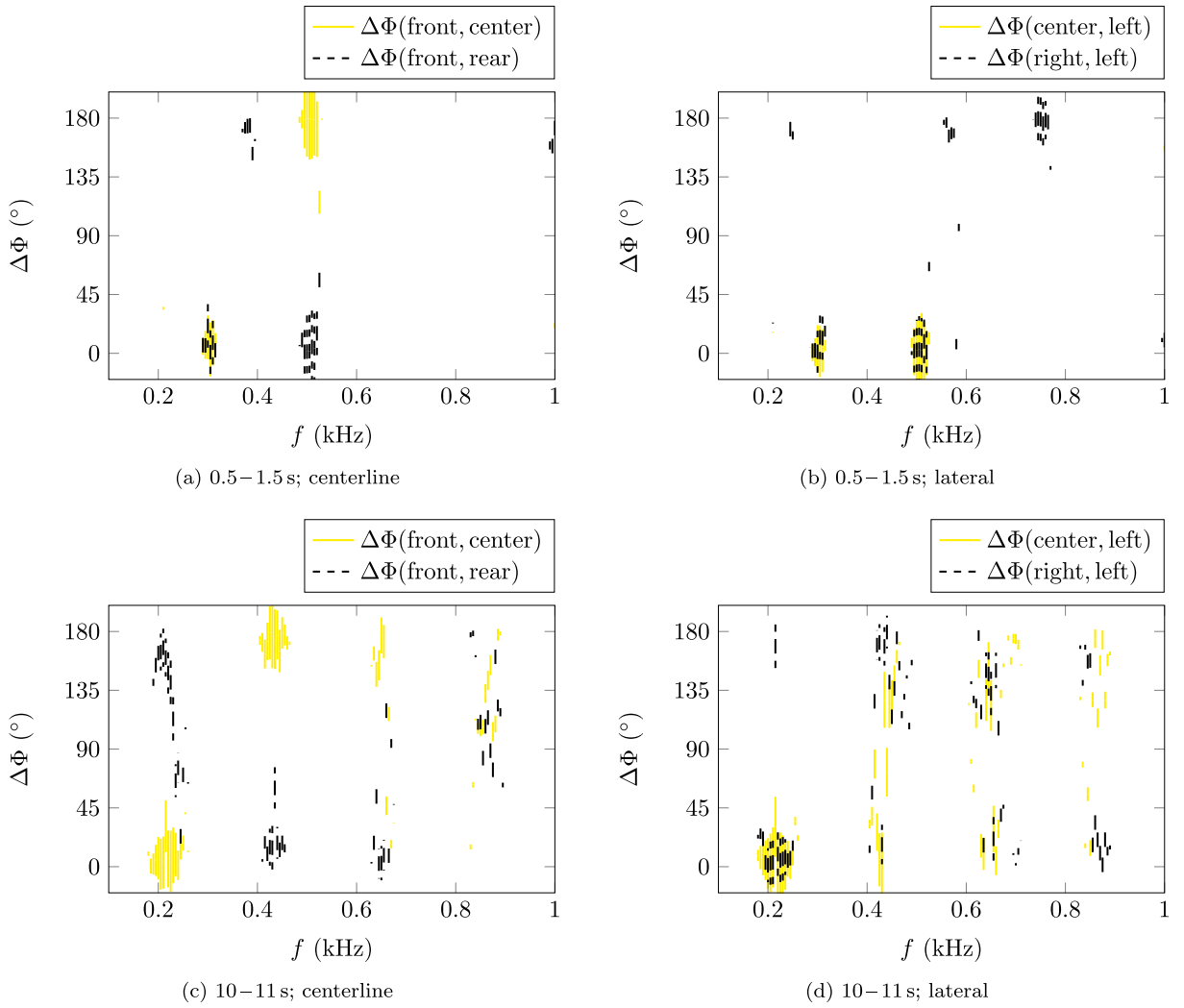

(a) 0.5 – 1.5 s; centerline

(b) 0.5 – 1.5 s; lateral

(c) 10 – 11 s; centerline

(d) 10 – 11 s; lateral

Fig. 19. Run 17 phase difference ($\Delta\Phi$) of the panel displacement for 0.7 mm panel and 20° shock generator.

To gain insight into the occurring structural modes, the phase content of the displacement signals was inspected. The phase difference ($\Delta\Phi$) between various sensor pairs was computed and weighted with the PSD of the measurements based on the approach described in [38]:

$$\Delta\Phi(a,b) := 180^\circ - \|180^\circ - |\Phi(a) - \Phi(b)|\| \tag{1}$$

$$\mathrm{PSD}_{mod}(a,b) := 8 \cdot \min(\max[c + \log(\mathrm{PSD}(a)), 0], \max[c + \log(\mathrm{PSD}(b)), 0]) \tag{2}$$

The cutoff (c) was set to 4 for run 13 and to 3 for run 17. Thus, in Figs. 17 and 19 values are only plotted where the exponent of the PSD exceeds the cutoff. PSD_{mod} is then plotted as vertical bar centered on $\Delta\Phi$. The results in both cases with 17.5° and 20° shock generator angle were computed for the time intervals 0.5 – 1.5 s and 10 – 11 s.

In the case with 17.5° shock generator, initially (Figs. 17a and 17b) dynamics occur near 300 Hz with all signals in phase indicative of a 0;0 mode. Near 400 Hz, dynamics are only detected at the front and rear position and not at any other with a phase difference of 180° which would correspond to a 1;0 mode. Near 500 Hz, dynamics are detected with a 180° phase difference of front and rear relative to center, left and right suggesting a 2;0 mode. The plots for 10 – 11 s (Figs. 17c and 17d) show that not only the occurring frequencies change as the panel heats up but also the occurring modes. At the lowest frequency, a phase difference of the rear signal of 180° with respect to all other positions appears but the 0;0 mode appears to be present as well. In combination with the spectrogram Fig. 16c, this suggests that these two modes occur at similar frequencies. This is presumably the explanation of the two branches observed near 200 Hz in the spectrogram. For dynamics at high frequencies, eg. near 800 Hz, in Figs. 17a and 17b, the case is less clear. This might be caused by the temporal averaging of the transient dynamics, e.g. the results at

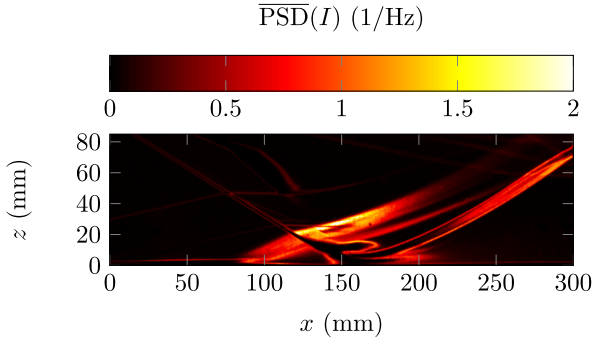

(a) Mean

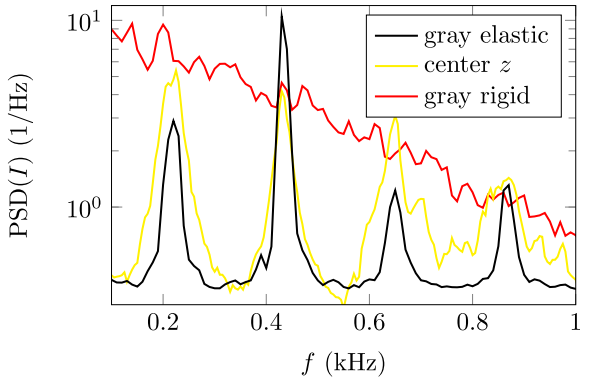

(b) Spectrum (PSD of center z and gray values from rigid case with arbitrary scale)

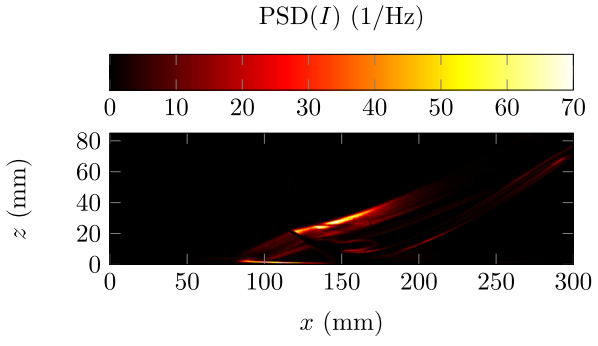

(c) 220 Hz

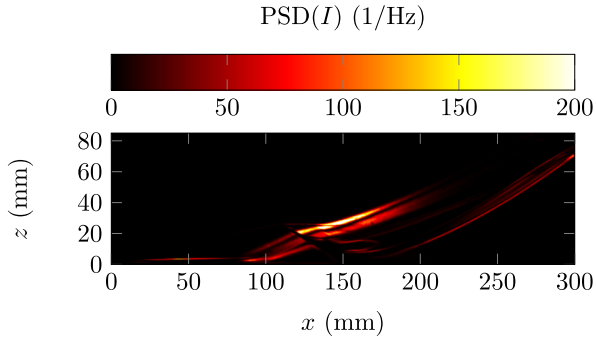

(d) 430 Hz

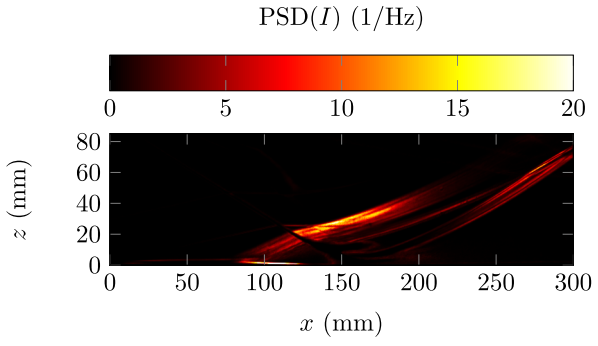

(e) 650 Hz

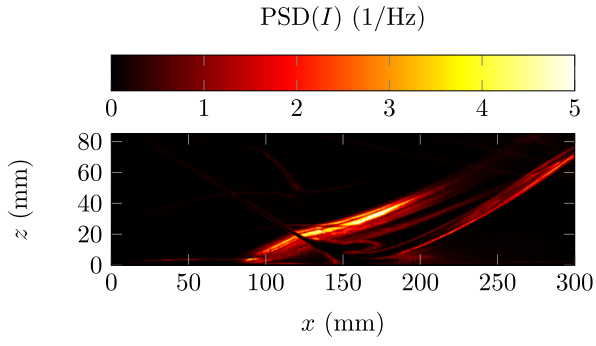

(f) 850 Hz

Fig. 20. PSD of gray values of shadowgraph images 20° shock generator.

around 800 Hz in Figs. 17a and 17b correspond to a large change in the occurring frequencies visible in the respective spectrogram (Fig. 16c).

Figs. 19a and 19b show that in the case with 20° shock generator similar to the previous case initially dynamics occur near 300 Hz with all signals in phase. Near 400 Hz and 500 Hz the behavior is also similar. Figs. 19c and 19d show the plots for 10 – 11 s where the panel has heated up in the course of the wind tunnel run. At slightly above 200 Hz, dynamics appear predominantly with the front, center, left and right sensors in phase but at a 180° difference to the rear sensor. Again at the higher frequencies substantial differences occur in the course of the wind tunnel run with the results being particularly unclear beyond 800 Hz.

Fig. 20 shows the PSD of gray values from high-speed shadowgraph recordings of the 20° shock generator case. Fig. 20a shows the mean value across the recorded flow field. It shows a structure similar to the rigid wall case (Fig. 19b), but with higher maximum amplitude. Also, the local maximum at the upstream side of the separation shock does not appear. This may be due to the up- and downstream movement of this shock caused by the movement of the panel. The distinct frequency peak connected the separation

Table 4
Computed panel modes for the 0.3 mm panel (number of neutral lines in x;y-direction).

Panel modes (Hz)										
0;0	1;0	2;0	0;1	1;1	1;1	4;0	2;1	3;1	5;0	5;0	4;1
277	320	386	470	536	562	570	607	670	684	752	806

shock movement in the rigid case could not be distinguished in the elastic cases. However, the spectrum of the gray values in the SWBLI area (Fig. 20b) shows very good agreement to the spectrum obtained from the panel displacement (center position from run 17, Fig. 18e) regarding the location of the peaks, underlining the direct coupling of structural and flow dynamics. The spectrum from the rigid case (Fig. 10a) was added to demonstrate that the rigid case shows a broad low frequency excitation while the elastic case matches the panel dynamics. The plots should be compared in terms of the occurring frequencies as the amplitude scaling is arbitrary. The PSD plots at discrete frequencies give some indication of how the structure influences the flow field. The plot at 220 Hz (Fig. 20c) indicates dynamics near the wall in the central part of the panel, while for 430 Hz (Fig. 20d) an effect can be seen on the upstream side of the panel. This mode appears to have the most significant impact on the Shadowgraph image presumably because it causes the biggest shift in position for the separation shock which is very well visible in the images. The effects are considerably smaller at 650 Hz and 850 Hz (Figs. 20e, 20f).

3.2.2. 0.3 mm panel

Figs. 21, 22 show the results obtained with the 0.3 mm panel. This panel was only used without shock generator. As with the 0.7 mm panel, the back pressure was adjusted to match the average pressure on the rigid insert, causing the panel to bend towards the test section before the run and returning to neutral position upon wind tunnel start-up. Again, the first second was used as reference to detect changes in structural dynamics and compare to an ANSYS solution (Table 4), obtaining good agreement for the lower modes (Fig. 21e). In all cases with nominal conditions, after tunnel start-up there are about 3 – 4 s with no dynamics, after which high amplitude oscillations of the panel begin (Figs. 21a, 21c, 21d) that are dominated by the first eigenmode (Fig. 22e). Between about 15 – 20 s, a change in maximum amplitude occurs, which appears to be connected to a change of the frequency of the oscillation (Fig. 22a) and also the average displacement (Fig. 22c).

A particularly interesting, however unintended, case is shown in Fig. 21b. For this run, the cover that protects the leading edge of the wind tunnel model between runs was left on, thus changing the geometry of the leading edge by adding a radius of several millimeters and a small backward facing step. While this is not a very well defined case, it is very instructive to observe how large a change in structural dynamics was caused by this. Firstly, oscillations throughout most of the experiment disappeared, except a few instances. Furthermore, the panel started to buckle much earlier and snapped through between different deformation shapes. As in the other runs, the deformation completely disappeared after shut-down of the flow and cool down of the model.

Similarly unintended but no less interesting are the results from run 26 (Fig. 21d). It starts out quite similar to the previous nominal runs, however, most notably at about 21 s, buckling (Fig. 22d) of an amplitude sufficient to stop panel dynamics occurs (Fig. 22b). The deformation fully receded after the run, leaving the panel in seemingly perfect condition. During a leak check after the run, it was found that the cavity would no longer hold pressure because air was venting through a failed part of the weld. Interestingly, the time of the failure does not coincide with the large change in deformation, but, as can be seen in the back pressure measurement, the behavior of the pressure changes at about 13 s, indicating that the failure started at that time. Before this run there was no obvious sign of an impending failure. Panel deformation fully receded after the previous run and the spectra at the beginning of the run also give no indication (Fig. 21f).

4. Discussion

The present experiments provide the first results on incident SWBLI interacting with a compliant panel in hypersonic flow, complementing a recent study by [63], who used a compression corner to obtain SWBLI. Several aspects are of particular interest:

- As shown numerically for supersonic flows at lower Mach numbers in [10,12], the presence of an incident shock of sufficient strength reduces the flutter boundary for such a configuration. This has been demonstrated in the present setup in hypersonic flow by a large variation of the incident shock angle, facilitating flutter for a configuration in which it would not occur for lower incident shock angles or in the absence of an incident shock. However, the contribution of the intrinsic unsteadiness of the SWBLI remains unclear in this context. Experiments and modeling suggest that, for a similar case at a lower Mach number, SWBLI dynamics do have an influence on the resulting panel dynamics [13,60,61]. The present results also show a strong effect of the dynamics of the elastic structure on the dynamics in the flow field visible in the high-speed shadowgraph recordings. In other studies in [38,63], setups were created that made it possible to look at the effect of SWBLI on a structure without flutter. This is an important contribution in this area but does not fully solve the problem of untangling combined cases with flutter and incident SWBLI with large flow separation.

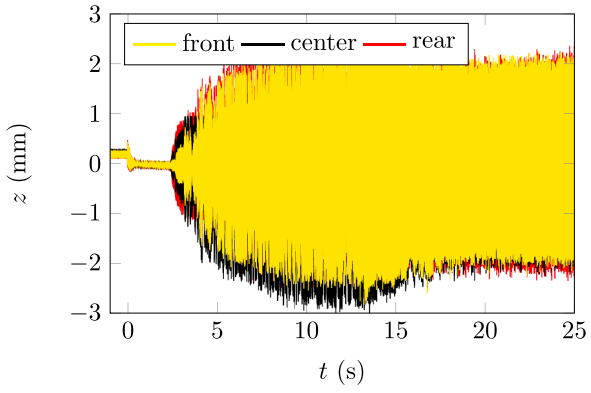

(a) Run 23 displacement

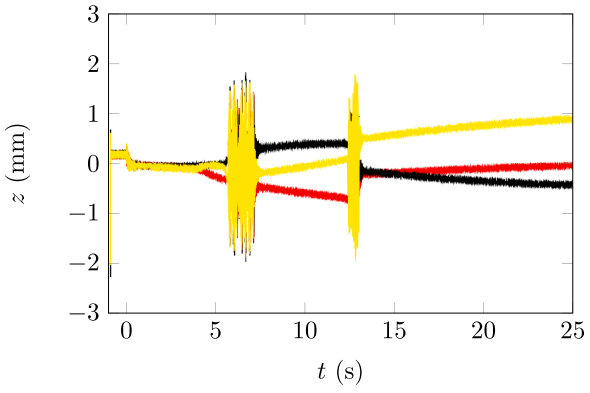

(b) Run 24 displacement (leading edge protective cover on)

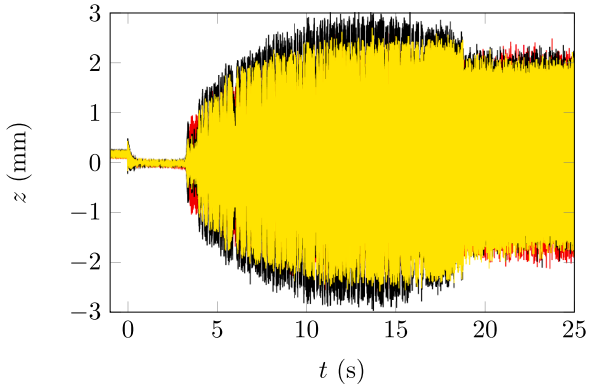

(c) Run 25 displacement

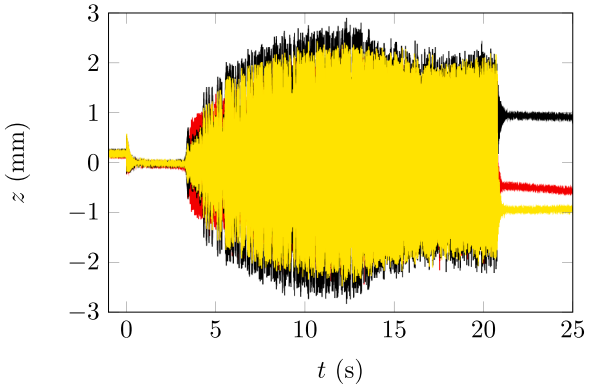

(d) Run 26 displacement (failure during run))

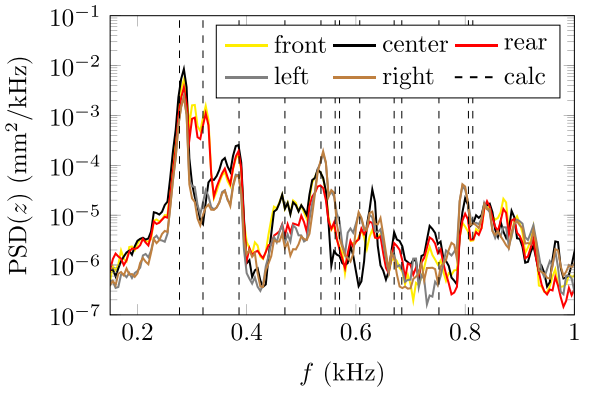

(e) Run 23 sensor displacement PSD 0.5 – 1.5 s

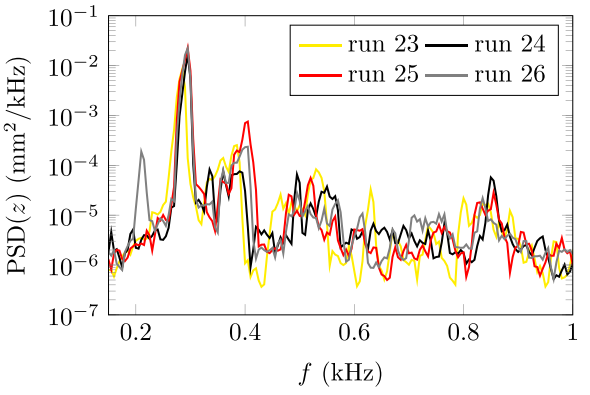

(f) Center sensor displacement PSD 0.5 – 1.5 s for run 23 – 26

Fig. 21. Panel displacement for 0.3 mm panel without shock generator (p_0 during run 25 was 1.7% and during run 26 was 1.6% below the nominal value).

- It is quite remarkable how very small changes in temperature can completely alter the dynamics of a structure in hypersonic flow. This has previously been shown for supersonic flows at lower Mach number, e.g. experimentally by [6] and theoretically by [79], also more recently numerically for hypersonic configurations (e.g. [80]). In most cases in literature, only the flutter boundaries were obtained and the post-flutter behavior was not investigated. From an aerodynamics point of view, this sensitivity to small temperature changes that was experimentally investigated for hypersonic flows in the present work means that reliable knowledge of the heat transfer to the structure is crucial, especially for flow fields that may include laminar–turbulent boundary layer transition or SWBLI. In the case of boundary layer transition, it may not be certain whether the flow

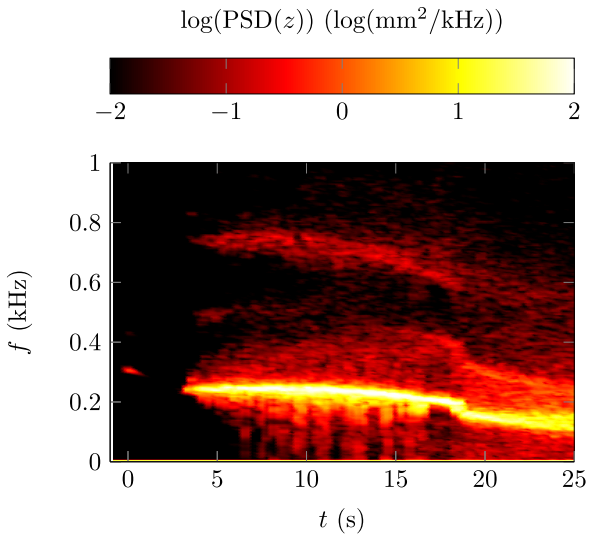

(a) Run 25 center displacement spectrogram

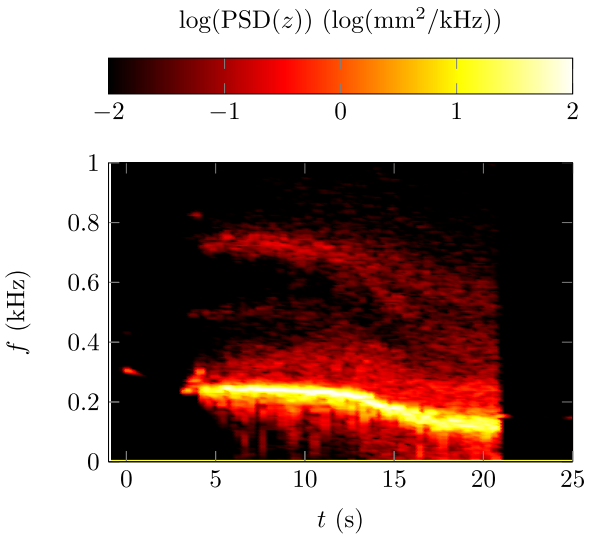

(b) Run 26 center displacement spectrogram

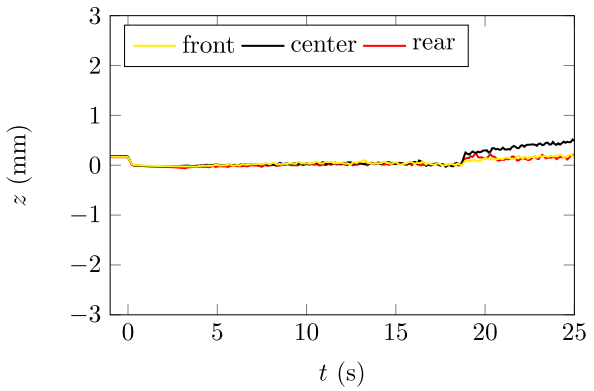

(c) Run 25 center displacement moving average

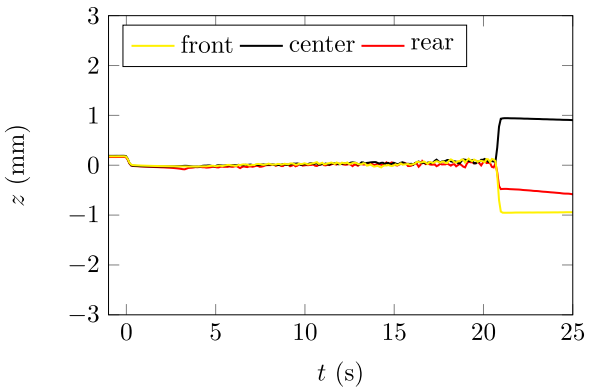

(d) Run 26 center displacement moving average

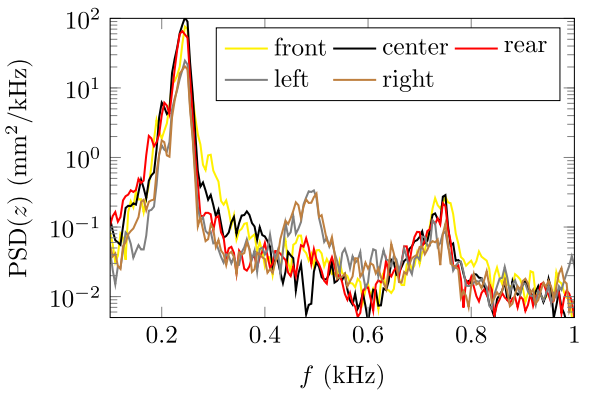

(e) Run 25 displacement PSD 10−11 s

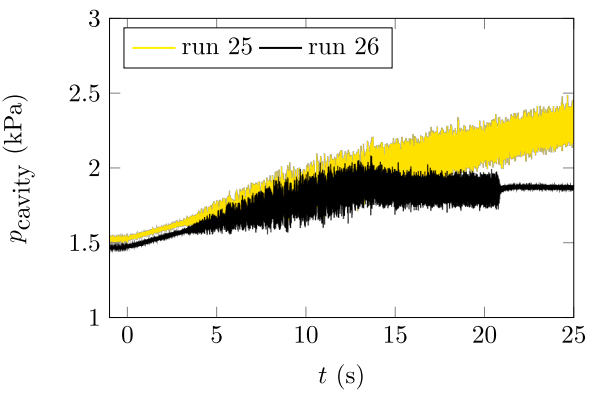

(f) Run 25, 26 cavity pressure

Fig. 22. Panel displacement spectrograms and moving average for 0.3 mm panel without shock generator.

is turbulent or laminar at a particular location, and in the transition region heat transfer may have a local maximum. But as the present experiments show, using the highest conceivable temperature as worst case estimate may very well be quite far from the worst case in terms of structural dynamics. Heating prediction for SWBLI cases can be even more prone to error as it relies on the properties of the incoming boundary layer and adds the complication of flow separation and in some cases resulting Görtler-like vortices [81,82]. Furthermore, changes in surface geometry drastically alter heat transfer (e.g. [41]) and surface pressure, making coupled treatment of such problems necessary.

- An area that deserves further attention is snap-through behavior of buckled structures as it has been observed here in some cases. This would certainly warrant focused studies such as have been begun in [14,24,46], where experiments on detailed dynamic characterization of structures under thermal loads were conducted. It would be very interesting to extend these studies by both numerical and wind tunnel investigations including a supersonic or hypersonic flow field.

- The demonstrated strong impact of small upstream disturbances of the flow field on structural dynamics is also a case that should certainly be subject to further research. The resulting studies might pose a challenging test case for advanced coupled modeling.

Research efforts in this area greatly benefit from a collaboration between experiments and modeling. With regards to aerodynamics modeling, it appears that a joint approach with simplified models and high-fidelity models is necessary as the former are not able to resolve the intricacies of turbulent flows while the latter typically do not reach physical time scales relevant for structural dynamics or heating. Improved understanding of these issues is crucial for the design of efficient and reliable vehicles operating in such domains, and in particular also for life-time prediction and structural health monitoring.

5. Conclusion

We conducted FSI experiments with and without incident SWBLI in hypersonic flow. In both cases, we obtained large panel dynamics that were strongly influenced by the thermal state of the structure. In several cases, aerothermal panel heating led to a degree of buckling sufficient to drastically reduce or stop panel dynamics, for which only small temperature changes were needed. For the case with incident shock, the results show that large incident shock angles facilitate flutter in configurations where it does not occur at lower shock angles or without incident shock. The dynamics in this case are related both to flutter and, presumably to a lesser extent, to the intrinsic SWBLI dynamics. However, these effects could not be separated. The SWBLI flow field on a rigid wall displayed significant dynamics below 1 kHz, which is the same order of magnitude as the characteristic frequencies of the panels. For the thinner panel, large amplitude flutter was obtained, leading to failure of this panel during the final wind tunnel run. Furthermore, it was observed that a small change in the model geometry upstream of the panel had a drastic impact on the resulting panel dynamics, leading to a near complete stop of oscillations and to snap-through events between different buckling shapes.

Declaration of competing interest

The authors declare that they have no known competing financial interests or personal relationships that could have appeared to influence the work reported in this paper.

Acknowledgments

Financial support was provided by the German Research Foundation (Deutsche Forschungsgemeinschaft – DFG) in the framework of the Sonderforschungsbereich Transregio 40 (SFB TRR40) “Fundamental Technologies for the Development of Future Space-Transport-System Components under High Thermal and Mechanical Loads”. The authors gratefully acknowledge the help and advice of the technical staff of the Supersonic and Hypersonic Technology Department and thank Burkard Esser and Daniel Kirchheck for their comments on the manuscript.

Appendix

The measurements using the PCB 132A31 pressure sensors for the case without incident shock (Fig. 23a) support the assessment of the state of the boundary layer from the infrared temperature measurements. The spectra resemble those typically obtained from a turbulent boundary layer (see e.g. [19]). A laminar boundary layer would produce considerably lower values. For the cases with incident shock (Figs. 23b – 23f), it can be seen that dynamics at these high frequencies, which are considerably higher than the frequencies in the order of 1 kHz that occur at the separation shock, increase with increasing incident shock angle by several orders of magnitude as has for example been shown in [57,59]. However, given this frequency range, this is considered out of scope for the present investigation.

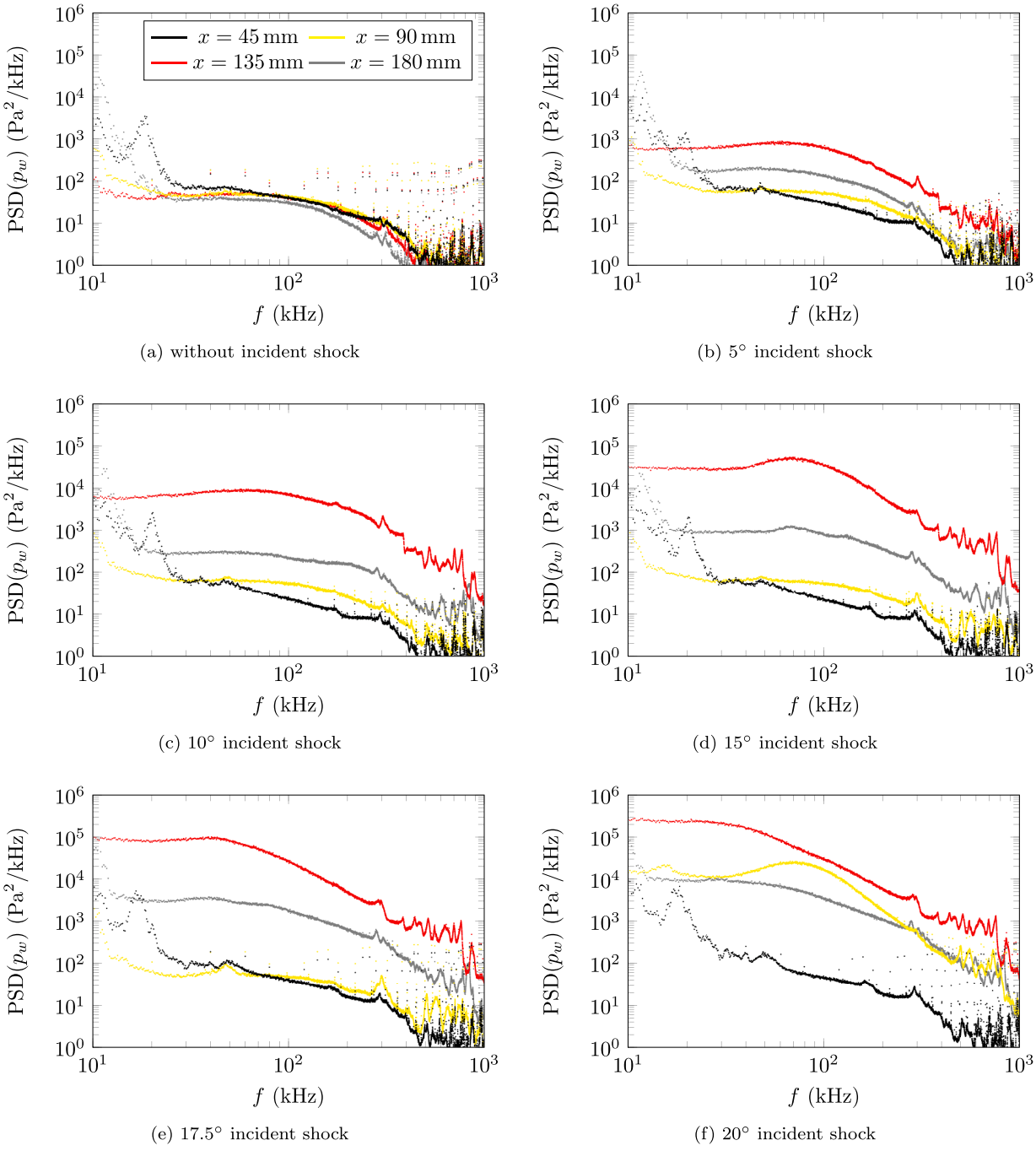

(a) without incident shock

(b) 5° incident shock

(c) 10° incident shock

(d) 15° incident shock

(e) 17.5° incident shock

(f) 20° incident shock

Fig. 23. High-frequency wall pressure dynamics on the rigid reference insert.

References

[1] J.D. Watts, Flight Experience with Shock Impingement and Interference Heating on the X-15-2 Research Airplane, Tech. Rep. TM X-1669, NASA, Flight Research Center, Edwards, Ca., 1968.

[2] G.H. Jordan, N.J. McLeod, L.D. Guy, Structural Dynamic Experiences of the X-15 Airplane, Tech. Rep. TN D-1158, NASA, Flight Research Center, Edwards, Ca., 1962.

[3] W. Koschel, Arianespace Flight 157 - Report of the Inquiry Board, Tech. rep., European Space Agency, 2003.

[4] S. Drogoul, From the Failure to the Success - The Return to Flight of the Ariane 5 ECA Launcher, in: 56th International Astronautical Congress, IAF, Fuduoka, Japan, 2005, http://dx.doi.org/10.2514/6.iac-05-d2.2.08.

[5] R. Bisplinghoff, Some Structural and Aeroelastic Considerations of High-Speed Flight - The Nineteenth Wright Brothers Lecture, J. Aeronaut. Sci. 23 (4) (1956) 289–329.

[6] E.E. Kordes, W.J. Tuovila, L.D. Guy, Flutter Research on Skin Panels, Tech. Rep. TN D-451, NASA, Langley Research Center, Langley Field, Va., 1960.

[7] D. Kontinos, Coupled Thermal Analysis Method with Application to Metallic Thermal Protection Panels, J. Thermophys. Heat Transfer 11 (2) (1997) 173–181, http://dx.doi.org/10.2514/2.6249.

[8] E.H. Dowell, in: L. Meirovitch (Ed.), Aeroelasticity of Plates and Shells, Noordhoff International Publishing, Leyden, Netherlands, 1975.

[9] J. Nichols, Final Report: Saturn V, S-IVB Panel Flutter Qualification Test, Tech. Rep. TN D-5439, NASA, George C. Marshall Space Flight Center, Marshall, Al., 1969.

[10] M. Visbal, On the interaction of an oblique shock with a flexible panel, J. Fluids Struct. 30 (2012) 219–225, http://dx.doi.org/10.1016/j.jfluidstructs.2012.02.002.

[11] E.H. Dowell, Aerodynamic Boundary Layer Effects on Flutter and Damping of Plates, J. Aircr. 10 (12) (1973) 734–738, http://dx.doi.org/10.2514/3.60298.

[12] M. Visbal, Viscous and inviscid interactions of an oblique shock with a flexible panel, J. Fluids Struct. 48 (2014) 27–45, http://dx.doi.org/10.1016/j.jfluidstructs.2014.02.003.

[13] S.M. Spottswood, T.J. Beberniss, T.G. Eason, R.A. Perez, J.M. Donbar, D.A. Ehrhardt, Z.B. Riley, Exploring the response of a thin, flexible panel to shock-turbulent boundary-layer interactions, J. Sound Vib. 443 (2019) 74–89, http://dx.doi.org/10.1016/j.jsv.2018.11.035.

[14] H.-G. Kim, R. Wiebe, Experimental and numerical investigation of nonlinear dynamics and snap-through boundaries of post-buckled laminated composite plates, J. Sound Vib. 439 (2019) 362–387, http://dx.doi.org/10.1016/j.jsv.2018.09.056.

[15] T.L. Lewis, N.J. McLeod, Flight Measurements of Boundary-Layer Noise on the X-15, Tech. Rep. TN D-3364, NASA, Flight Research Center, Edwards, Ca., 1966.

[16] C.F. Coe, W.J. Chyu, Pressure-Fluctuation Inputs and Response of Panels Underlying Attached and Separated Supersonic Turbulent Boundary Layers, Tech. Rep. TM X-62,189, NASA, Ames Research Center, Moffett Field, Ca., 1972.

[17] D.S. Dolling, Fifty Years of Shock-Wave/Boundary-Layer Interaction Research: What Next? AIAA J. 39 (8) (2001) 1517–1531, http://dx.doi.org/10.2514/2.1476.

[18] H. Schlichting, K. Gersten, Boundary-Layer Theory, Springer, Berlin, Heidelberg, 2017, http://dx.doi.org/10.1007/978-3-662-52919-5.

[19] S. Willems, A. Gülhan, J. Steelant, Experiments on the Effect of Laminar-Turbulent Transition on the SWBLI in H2K at Mach 6, Exp. Fluids (2015) 1–19, http://dx.doi.org/10.1007/s00348-015-1904-z.

[20] B.M. Wheaton, D.C. Berridge, T.D. Wolf, R.T. Stevens, B.E. McGrath, Boundary Layer Transition (BOLT) Flight Experiment Overview, in: 2018 Fluid Dynamics Conference, American Institute of Aeronautics and Astronautics, Atlanta, Ga., 2018, http://dx.doi.org/10.2514/6.2018-2892.

[21] V. Shinde, J. McNamara, D. Gaitonde, C. Barnes, M. Visbal, Transitional shock wave boundary layer interaction over a flexible panel, J. Fluids Struct. 90 (2019) 263–285, http://dx.doi.org/10.1016/j.jfluidstructs.2019.07.007.

[22] P.S. Volpiani, M. Bernardini, J. Larsson, Effects of a nonadiabatic wall on hypersonic shock/boundary-layer interactions, Phys. Rev. Fluids 5 (1) (2020) http://dx.doi.org/10.1103/physrevfluids.5.014602.

[23] V. Pasquariello, Analysis and Control of Shock-Wave/Turbulent Boundary-Layer Interactions on Rigid and Flexible Walls (Ph.D. thesis), Technische Universität München, 2018.

[24] B. Miller, J. McNamara, S. Spottswood, A. Culler, The impact of flow induced loads on snap-through behavior of acoustically excited, thermally buckled panels, J. Sound Vib. 330 (23) (2011) 5736–5752, http://dx.doi.org/10.1016/j.jsv.2011.06.028.

[25] S. Bouslog, B. Moore, I. Lawson, J. Sawyer, X-33 Metallic TPS Tests in NASA-LARC High Temperature Tunnel, in: 37th Aerospace Sciences Meeting and Exhibit, American Institute of Aeronautics and Astronautics, Reno, Nv., 1999, http://dx.doi.org/10.2514/6.1999-1045.

[26] E. Musk, Making Life Multi-Planetary, New Space 6 (1) (2018) 2–11, http://dx.doi.org/10.1089/space.2018.29013.emu.

[27] C. Mei, K. Abdel-Motagaly, R. Chen, Review of Nonlinear Panel Flutter at Supersonic and Hypersonic Speeds, Appl. Mech. Rev. 52 (10) (1999) 321–332, http://dx.doi.org/10.1115/1.3098919.

[28] O.J. Haidn, N.A. Adams, R. Radespiel, T. Sattelmayer, W. Schröder, C. Stemmer, B. Weigand, Future space-transport-system components under high thermal and mechanical loads, in: N. Adams, W. Schröder, R. Radespiel, O. Haidn, T. Sattelmayer, C. Stemmer, B. Weigand (Eds.), Notes on Numerical Fluid Mechanics and Multidisciplinary Design, 2021, pp. 1–30, http://dx.doi.org/10.1007/978-3-030-53847-7_1, Ch. Collaborative Research for Future Space Transportation Systems.

[29] W.H. Stillwell, X-15 Research Results - With a Selected Bibliography, Tech. Rep. SP-60, NASA, Washington, D.C., 1965.

[30] J.M. Jenkins, R.D. Quinn, A Historical Perspective of the YF-12A Thermal Loads and Structures Program, Tech. Rep. TM 104317, NASA, Dryden Flight Research Center, Edwards, Ca., 1996.

[31] P.W. Merlin, Design and Development of the Blackbird: Challenges and Lessons Learned, in: 47th AIAA Aerospace Sciences Meeting Including the New Horizons Forum and Aerospace Exposition, no. AIAA 2009-1522, AIAA, Orlando, Fl., 2009.

[32] T.R. Lall, Interstage Adapter Panel Flutter on Atlas-Centaur AC-2, AC-3, and AC-4 Vehicles, Tech. Rep. TM X-1179, NASA, Lewis Reserach Center, Cleveland, Oh., 1965.

[33] M.L. Nacht, R.L. Greene, Panel Flutter Studies of Boost-Vehicle Full-Scale Flight Insulation Panels, Tech. Rep. TM X-1417, NASA, Lewis Research Center, Cleveland, Oh., 1967.

[34] S.C. Krausse, Saturn V Aerothermodynamics Flight Evaluation Summary AS-501 through AS-503, Tech. Rep. D5-15796-1, The Boeing Company, 1969.

[35] T.M. Perkins, Aeroelastic Stability of an Array of Full-Scale Panels from the Saturn S-IVB Stage at Transonic Mach Numbers, Tech. Rep. AEDC-TR-67-9, Arnold Engineering Development Center, Arnold Air Force Station, Tn., 1967.

[36] E.H. Hirschel, Basics of Aerothermodynamics, Springer-Verlag, Berlin, Heidelberg, New York, 2005.

[37] S. Willems, B. Esser, A. Gülhan, Experimental and numerical investigation on thermal fluid-structure interaction on ceramic plates in high enthalpy flow, CEAS Space J. 7 (4) (2015) 483–497, http://dx.doi.org/10.1007/s12567-015-0101-5.

[38] S. Willems, Strömung-Struktur-Wechselwirkung in Überschallströmungen (Fluid/Structure Interaction in Supersonic Flows) (Ph.D. thesis), DLR/RWTH Aachen University, 2017, URL https://elib.dlr.de/116735/.

[39] R. Niesner, Gekoppelte Simulation thermisch-mechanischer Fluid-Struktur-Interaktionen für Hyperschall-Anwendungen (Coupled Simulation of Thermomechanical Fluid-Structure Interaction for Hypersonic Applications) (Ph.D. thesis), Technische Universität Braunschweig, 2009.

[40] M. Haupt, R. Niesner, B. Esser, A. Gülhan, Model Configuration for the Validation of Aerothermodynamic Thermal- Mechnical Fluid-Structure-Interactions, in: Proceedings of the ASME 2012 11th Biennial Conference on Engineering Systems Design and Analysis, no. ESDA2012/82908, Nantes, France, 2012.

[41] D. Daub, B. Esser, A. Gülhan, Experiments on High-Temperature Hypersonic Fluid-Structure Interaction with Plastic Deformation, AIAA J. 58 (4) (2020) 1423–1431, http://dx.doi.org/10.2514/1.j059150.

[42] K. Martin, D. Daub, B. Esser, A. Gülhan, S. Reese, Future Space-Transport-System Components under High Thermal and Mechanical Loads, in: N. Adams, W. Schröder, R. Radespiel, O. Haidn, T. Sattelmayer, C. Stemmer, B. Weigand (Eds.), Notes on Numerical Fluid Mechanics and Multidisciplinary Design, 2021, pp. 341–355, http://dx.doi.org/10.1007/978-3-030-53847-7_22, Ch. Numerical Modelling of Fluid-Structure Interaction for Thermal Buckling in Hypersonic Flow.

[43] E.A. Thornton, J.T. Oden, W.W. Tworzydlo, S.-K. Youn, Thermoviscoplastic Analysis of Hypersonic Structures Subjected to Severe Aerodynamic Heating, J. Aircr. 27 (9) (1990) 826–835, http://dx.doi.org/10.2514/3.45943.

[44] E.A. Thornton, P. Dechaumphai, Coupled Flow, Thermal, and Structural Analysis of Aerodynamically Heated Panels, J. Aircr. 25 (11) (1988) 1052–1059, http://dx.doi.org/10.2514/3.45702.

[45] D.A. Kontinos, G. Palmer, Numerical Simulation of Metallic Thermal Protection System Panel Bowing, J. Spacecr. Rockets 36 (6) (1999) 842–849, http://dx.doi.org/10.2514/2.3523.

[46] D.A. Ehrhardt, L.N. Virgin, Experiments on the thermal post-buckling of panels, including localized heating, J. Sound Vib. 439 (2019) 300–309, http://dx.doi.org/10.1016/j.jsv.2018.08.043.

[47] E.H. Dowell, H.M. Voss, The Effect of a Cavity on Panel Vibration, AIAA J. 1 (2) (1963) 476–477, http://dx.doi.org/10.2514/3.1568.

[48] J.L. Shideler, S.C. Dixon, C.P. Shore, Flutter at Mach 3 of Thermally Stressed Panels and Comparison with Theory for Panels with Edge Rotational Restraint, Tech. Rep. TN D-3498, NASA, Langley Research Center, Langley Station, Hampton, Va., 1966.

[49] C.S. Ventres, E.H. Dowell, Comparison of Theory and Experiment for Nonlinear Flutter of Loaded Plates, AIAA J. 8 (11) (1970) 2022–2030, http://dx.doi.org/10.2514/3.6041.

[50] H.P. Kappus, C.E. Lemley, N.H. Zimmermann, An Experimental Investigation of High Amplitude Panel Flutter, Tech. Rep. CR-1837, NASA, McDonnell Douglas Corporation, St. Louis, Mo. for George C. Marshall Space Flight Center, Al., 1971, p. 129.

[51] M. Freydin, E.H. Dowell, S.M. Spottswood, R.A. Perez, Nonlinear dynamics and flutter of plate and cavity in response to supersonic wind tunnel start, Nonlinear Dynam. (2020) http://dx.doi.org/10.1007/s11071-020-05817-x.

[52] R. Wiebe, S. Spottswood, On the dimension of complex responses in nonlinear structural vibrations, J. Sound Vib. 373 (2016) 192–204, http://dx.doi.org/10.1016/j.jsv.2016.03.009.

[53] L. Maestrello, Radiation from and Panel Response to a Supersonic Turbulent Boundary Layer, J. Sound Vib. 10 (2) (1969) 261–295, http://dx.doi.org/10.1016/0022-460X(69)90200-4.

[54] L. Maestrello, T.L.J. Linden, Measurements of the Response of a Panel Excited by Shock Boundary-Layer Interaction, J. Sound Vib. 16 (3) (1971) 385–391, http://dx.doi.org/10.1016/0022-460X(71)90594-3.

[55] N.T. Clemens, V. Narayanaswamy, Low-Frequency Unsteadiness of Shock Wave/Turbulent Boundary Layer Interactions, Annu. Rev. Fluid Mech. 46 (1) (2014) 469–492, http://dx.doi.org/10.1146/annurev-fluid-010313-141346.

[56] S. Willems, A. Gülhan, B. Esser, Shock Induced Fluid-Structure Interaction on a Flexible Wall in Supersonic Turbulent Flow, Prog. Flight Phys. 5 (2013) 285–308, http://dx.doi.org/10.1051/eucass/201305.

[57] D. Daub, S. Willems, A. Gülhan, Experiments on the Interaction of a Fast-Moving Shock with an Elastic Panel, AIAA J. 54 (2) (2016) 670–678, http://dx.doi.org/10.2514/1.J054233.

[58] V. Pasquariello, S. Hickel, N. Adams, G. Hammerl, W.A. Wall, D. Daub, S. Willems, A. Gülhan, Coupled simulation of shock-wave/turbulent boundary-layer interaction over a flexible panel, in: 6th European Conference for Aerospace Sciences, EUCASS, Krakow, Poland, 2015.

[59] V. Pasquariello, S. Hickel, N.A. Adams, Unsteady effects of strong shock-wave/boundary-layer interaction at high Reynolds number, J. Fluid Mech. 823 (2017) 617–657, http://dx.doi.org/10.1017/jfm.2017.308.

[60] A. Gogulapati, R. Deshmukh, A.R. Crowell, J.J. McNamara, V. Vyas, X.Q. Wang, M. Mignolet, T. Beberniss, S.M. Spottswood, T.G. Eason, Response of a Panel to Shock Impingement: Modeling and Comparison with Experiments, in: 55th AIAA/ASME/ASCE/AHS/ASC Structures, Structural Dynamics, and Materials Conference, American Institute of Aeronautics and Astronautics, National Harbor, Md., 2014, http://dx.doi.org/10.2514/6.2014-0148.

[61] A. Gogulapati, R. Deshmukh, J.J. McNamara, V. Vyas, X. Wang, M.P. Mignolet, T. Beberniss, S.M. Spottswood, T.G. Eason, Response of a Panel to Shock Impingement: Modeling and Comparison with Experiments - Part 2, in: 56th AIAA/ASCE/AHS/ASC Structures, Structural Dynamics, and Materials Conference, American Institute of Aeronautics and Astronautics, Kissimmee, Fl., 2015, http://dx.doi.org/10.2514/6.2015-0685.

[62] A. Tripathi, L. Mears, K. Shoele, R. Kumar, Oblique Shockwave Boundary Layer Interactions on a Flexible Panel at Mach 2, in: AIAA Scitech 2020 Forum, American Institute of Aeronautics and Astronautics, Orlando, Fl., 2020, http://dx.doi.org/10.2514/6.2020-0568.

[63] T.J. Whalen, A.G. Schöneich, S.J. Laurence, B.T. Sullivan, D.J. Bodony, M. Freydin, E.H. Dowell, G.M. Buck, Hypersonic Fluid–Structure Interactions in Compression Corner Shock-Wave/Boundary-Layer Interaction, AIAA J. 58 (9) (2020) 4090–4105, http://dx.doi.org/10.2514/1.j059152.

[64] H.T. Pham, Z.N. Gianikos, V. Narayanaswamy, Compression Ramp Induced Shock-Wave/Turbulent Boundary-Layer Interactions on a Compliant Material, AIAA J. (2018) 1–5, http://dx.doi.org/10.2514/1.j056652.

[65] A. Hashimoto, T. Aoyama, Y. Nakamura, Effects of Turbulent Boundary Layer on Panel Flutter, AIAA J. 47 (12) (2009) 2785–2791, http://dx.doi.org/10.2514/1.35786.

[66] K.M. Casper, S.J. Beresh, J.F. Henfling, R.W. Spillers, P. Hunter, S. Spitzer, Hypersonic Fluid-Structure Interactions Due to Intermittent Turbulent Spots on a Slender Cone, AIAA J. 57 (2) (2019) 749–759, http://dx.doi.org/10.2514/1.j057374.

[67] F.-J. Niezgodka, Der Hyperschallwindkanal H2K des DLR in Köln-Porz (The Hypersonic Wind Tunnel H2K of DLR in Köln-Porz), DLR, Cologne, Germany, 2001.

[68] Equations, Tables, and Charts for Compressible Flow, Tech. Rep. 1135, National Advisory Committee for Aeronautics, 1953.

[69] CODATA Recommended Values of the Fundamental Physical Constants: 2018, Tech. Rep. NIST SP 961, National Institute of Standards and Technoloy, 2019, URL https://physics.nist.gov/cuu/pdf/wall_2018.pdf.

[70] S. Willems, User Guide: ROBOT 8.8 - Render Object Based Orientation Tracking, DLR, Cologne, Germany, 2019.

[71] A. Henckels, P. Gruhn, Study on Aerothermal Effects of Viscous Shock Interaction in Hypersonic Inlets, in: Proceedings of the Fifth European Symposium on Aerothermodynamics for Space Vehicles, no. ESA SP-563, European Space Agency, Cologne, Germany, 2005.

[72] R.H. Korkegi, Hypersonic Aerodynamics, Von Karman Institute for Fluids Dynamics, Rhode-Saint-Genese, Belgium, 1962.

[73] P. Welch, The Use of Fast Fourier Transform for the Estimation of Power Spectra: A Method Based on Time Averaging Over Short, Modified Periodograms, IEEE Trans. Audio Electroacoust. 15 (2) (1967) 70–73, http://dx.doi.org/10.1109/TAU.1967.1161901.

[74] P.A. Polivanov, A.A. Sidorenko, A.A. Maslov, Experimental Study of Unsteady Effects in Shock Wave / Turbulent Boundary Layer Interaction, in: 47th AIAA Aerospace Sciences Meeting Including the New Horizons Forum and Aerospace Exposition, American Institute of Aeronautics and Astronautics, Orlando, Fl., 2009, http://dx.doi.org/10.2514/6.2009-409.

[75] D. Kirchheck, D. Saile, A. Gülhan, Spectral Analysis of Rocket Wake Flow-Jet Interaction by Means of High-Speed Schlieren Imaging, in: Proceedings of the 8th European Conference for Aeronautics and Space Sciences, Madrid, 2019. http://dx.doi.org/10.13009/EUCASS2019-1057.

[76] Z. Sun, T. Gan, Y. Wu, Shock-Wave/Boundary-Layer Interactions at Compression Ramps Studied by High-Speed Schlieren, AIAA J. 58 (4) (2020) 1681–1688, http://dx.doi.org/10.2514/1.j058257.
[77] Datasheet: Deutsche Edelstahlwerke – X5CrNi18-10 1.4301 (recieved 14.7.2021), 2021.
[78] A. Henckels, A. Kreins, F. Maurer, Experimental investigations of hypersonic shock-boundary layer interaction, Z. Flugwiss. Weltraumforsch. 17 (1993) 116–124.
[79] E.H. Dowell, Panel Flutter – A review of the Aeroelastic Stability of Plates and Shells, AIAA J. 8 (3) (1970) 385–399, http://dx.doi.org/10.2514/3.5680, URL http://arc.aiaa.org/doi/abs/10.2514/3.5680.
[80] I.H. Nydick, Studies in Hypersonic Aeroelasticity (Ph.D. thesis), University of California, Los Angeles, Ca., 2000.
[81] A.F. Kreins, A. Henckels, F. Maurer, Experimental studies of hypersonic shock induced boundary layer separation, Z. Flugwiss. Weltraumforsch. 2 (20) (1996) 80–88.
[82] G.M.D. Currao, R. Choudhury, S.L. Gai, A.J. Neely, D.R. Buttsworth, Hypersonic Transitional Shock-Wave–Boundary-Layer Interaction on a Flat Plate, AIAA J. 58 (2) (2020) 814–829, http://dx.doi.org/10.2514/1.j058718.